

Electrical Impedance Tomography for Cardiovascular Imaging and Monitoring

by

Symon Stowe

A thesis submitted in partial fulfillment of the requirements for the
degree of

Ph.D.

in

Biomedical Engineering

Carleton University

Ottawa, Ontario

© 2021

Symon Stowe

To ...

Abstract

This thesis serves to show the background, methods, planned methods and timeline for the final thesis. The thesis will consist of 6 chapters, in introduction to give background and motivation for the research

Acknowledgements

Write here

Contents

Abstract	i
Acknowledgements	i
Contents	vi
List of Figures	vii
List of Tables	ix
list of Acronyms	x
1 Introduction	1
1.1 Problem Statement	2
1.2 Thesis objectives	2
1.3 Contributions	2
2 Background	3
2.1 Electrical Impedance Tomography	3

2.1.1	Impedance Imaging	3
2.1.2	Bioimpedance	4
2.1.3	Forward Problem	5
2.1.4	Discretization and the Finite Element Method	5
2.1.5	Image Reconstruction	5
2.1.5.1	2D reconstruction	5
2.1.5.2	3D Reconstruction	5
2.1.5.3	GREIT	6
2.1.5.4	Image Regularization	6
2.1.6	Internal Electrodes	6
2.1.6.1	Internal Reference Electrodes	6
2.1.6.2	Inverse Source localization (time permitting)	6
2.1.7	Imaging Techniques	6
2.1.7.1	Absolute	6
2.1.7.2	Frequency Difference	7
2.1.7.3	Time Difference	7
2.2	Lung perfusion monitoring	7
2.2.1	Sensitivity to Blood Movement	7
2.2.2	Contrast agent injection	7
2.2.3	Frequency Filtering	7
2.3	Aortic flow monitoring	10

3 Comparison of bolus- and filtering-based EIT measures of lung perfusion in an animal model 13

3.1	Summary	13
3.2	Introduction	14
3.3	Methods	18
3.3.1	Overview	18
3.3.2	Animals	18
3.3.3	Data Acquisition and Image Reconstruction	19
3.3.4	Functional EIT Images	21
3.3.4.1	Bolus injection image (P_B)	22
3.3.4.2	Frequency-Filtering	23
3.3.4.3	Ensemble Averaging	24
3.3.5	Image Comparison	26
3.3.6	Statistical Analysis	27
3.4	Results	27
3.5	Discussion	29
4	FEM mesh refinement for 3D Electrical Impedance Tomography	35
4.1	Summary	35
4.2	Introduction	36
4.3	METHODS	38
4.3.1	Overview	38
4.3.2	Mesh Generation	38
4.3.3	Simulation	42
4.3.4	Electrode refinement for arbitrary FEMs	45
4.4	Results	46

4.5	Discussion	50
4.6	Conclusion	53
5	Custom Meshes from CT Images	54
5.1	EIT for ARDS Patients	55
5.2	A Segment Editor Program	55
5.2.1	Automatic segmentation of the thorax	55
5.2.2	Manual Segmentation Correction	56
5.2.3	Mesh Generation	56
5.2.3.1	Extruded Geomerty	56
5.2.3.2	3D Lung Regions	56
5.3	Evaluation on ARDS Patients	56
5.3.1	Methods	56
5.3.2	Results	56
6	Internal Electrodes	59
6.1	Motivation	59
6.2	Summary	60
6.3	Simulations	60
6.4	Phantom Measurements	67
6.5	Motion Correction	68
6.6	Inverse Source Localization	68
6.7	Animal Data	68
6.8	Methods	68

6.9	Conclusions	70
7	Conclusion	71
7.1	Summary of Findings	71
7.2	Future Work	71
	Bibliography	72

List of Figures

2.1	Current and Equipotential lines	4
3.1	Overview of the EIT analysis methods	20
3.2	Selection of the bolus signal	23
3.3	Frequency analysis methods	25
3.4	Ensemble averaging analysis	26
3.5	Jaccard index scores	28
3.6	Example perfusion images	30
4.1	Example meshes for various refinement strategies	40
4.2	Mesh size surrounding the electrode	41
4.3	Balance point calculation method	43
4.4	Mesh sensitivity error vs. elements per electrode	47
4.5	Sensitivity distribution and regions of interest	48
4.6	Sensitivity error with shifting node balance	49
4.7	Advanced mesh example of an internal probe	52
5.1	Single breath using: A) generic model B) custom model	57

5.2 An overview of the segmentation and editing process showing: A) A sample raw CT which was thresholded, scaled and adjusted over several adjacent slices to identify the lung regions and an enclosed rib area, and the resulting lung estimate; and B) A screen capture of the manual mesh correction process and 2 views of the generated mesh.	58
6.1 Internal electrode configurations	61
6.2 Internal electrode simulation reconstructions	62
6.3 Sensitivity with different internal electrode configurations	63
6.4 Current injection patterns with internal electrodes	65
6.5 Sensitivity using internal electrodes with modified injection patterns .	66
6.6 Sensitivity distribution in a lamb model	69
6.7 Reconstructed image of a single breath	70

List of Tables

4.1	Parameters used to generate meshes	44
5.1	Ventilated lung estimate vs. GI index scores.	57

Chapter 1

Introduction

Electrical impedance tomography (EIT) is an imaging modality that uses an arrangement of electrodes to simultaneously apply stimulation currents and measure the resulting electric potentials. Measurements of potential at the electrodes are used in conjunction with prior information to reconstruct images of the internal conductivity. In biomedical applications, the variance in conductivity between different tissue types and fluids within the body enables non-invasive imaging of functional activity using electrodes on the body surface.

As electrical current travels through the body it diffuses away from the electrodes, travelling in three dimensions along the path of least resistance. EIT is most sensitive to impedance changes close to the electrodes and along the path of the injected current. This document proposes a thesis that investigates the use of novel 3D electrode configurations and injection patterns to maximize sensitivity and improve continuous monitoring of cardiopulmonary measures using EIT.

1.1 Problem Statement

1.2 Thesis objectives

The following questions will be answered by the thesis:

1. How do current methods of EIT lung perfusion imaging compare? (*Chapter 2*)
2. What advantages can internal electrode configurations provide? (*Chapter 3*)
3. What advantage do alternative external electrode configurations provide when monitoring aortic blood flow? (*Chapter 4*)
4. How can a configuration that is better able to isolate cardiac activity improve measures of lung perfusion and aortic flow in an animal model? (*Chapter 5*)

1.3 Contributions

Chapter 2

Background

this is short and needs a lot more detail and also figures.

This section briefly reviews the current techniques for lung perfusion and hemodynamic monitoring, and provides a general overview of the state of 3D EIT as used for thoracic imaging and monitoring.

2.1 Electrical Impedance Tomography

2.1.1 Impedance Imaging

Impedance imaging has been in use since the early 1900s for geophysical applications. Originally introduced as a technique to image below the earth's surface, current was transmitted between two electrodes placed into the ground and any anomalies in subsurface conductivity produced deviation in the equipotential lines. Including current injections and measurements from multiple locations and using known elec-

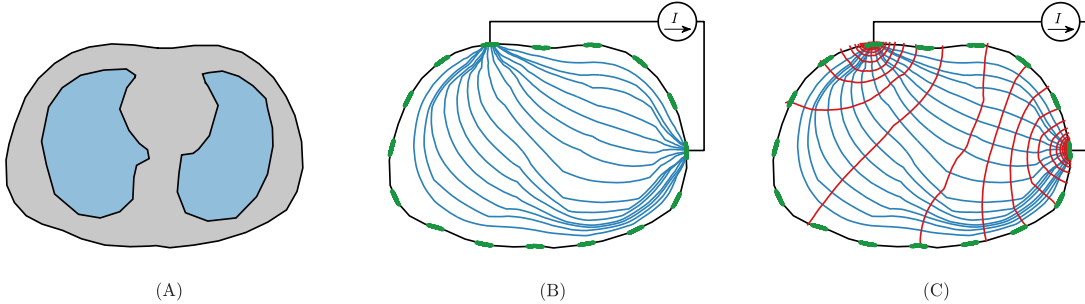


Figure 2.1: (A) A body comprising tissues of different conductivity, (B) Electrodes are placed on the surface and current is injected between a pair of electrodes. The current pathways are indicated by the blue lines. (C) The resulting equipotential lines within the body.

trical properties of geological structures Conrad Schlumberger identified features of underground geological structures (Allaud and Martin, 1977).

These same techniques can be applied in biomedical applications where voltage is measured on an array of body surface electrodes while current is applied between select electrode pairs(figure 2.1). Due to impedance differences associated with biological tissues and their physiological function (**Geddes1967; McAdams1995**) EIT has been proposed for a wide range of applications from thoracic monitoring to neuronal and brain imaging (**Holder1992; Frerichs2016**).

2.1.2 Bioimpedance

TODO:

Discuss high and low frequencies and the impedance of the tissues of interest

What constraints are easy and which are interesting?

2.1.3 Forward Problem

Using the quasi-static formulations of Maxwell's equations, the potential distribution u can be used compute the conductivity ρ and generate images.

2.1.4 Discretization and the Finite Element Method

2.1.5 Image Reconstruction

2.1.5.1 2D reconstruction

2.1.5.2 3D Reconstruction

The majority of EIT measurements are done with a single ring of external electrodes but in practice, electrical current cannot be confined to a single plane and using a two dimensional electrode configuration can significantly impact the capabilities of EIT (**Rabbani1991**). The use of 3D electrode configurations in EIT was introduced in 1996 (**Metherall1996**) to overcome the inherent limitations of 2D measurements, but it is still not widely used today. It is thought this is due to the increased complexity of 3D images and the subsequent analysis (**Grychtol2019**).

It has been shown that externally placed 3D electrode configurations consisting of two electrode planes can improve the sensitivity distribution and image quality (**Grychtol2016**), but there is still limited sensitivity in the central-most regions of the chest. The concept of using internal esophageal electrodes has been presented previously (**Pilkington1989; Schuessler1995**) as a method to improve internal sensitivity and reconstruction quality, but has not been widely used or simulated.

Several studies have shown that there may be several advantages to using an internal electrode in EIT recordings; Measurements with an internal electrode have been shown to reconstruct images equally as well as configurations with twice as many external electrodes (**Schuessler1995**), and have shown an increase in sensitivity in a central region of interest (**Kwon2013**; **Czaplik2014**; **Farooq2014**).

2.1.5.3 GREIT

2.1.5.4 Image Regularization

2.1.6 Internal Electrodes

2.1.6.1 Internal Reference Electrodes

2.1.6.2 Inverse Source localization (time permitting)

2.1.7 Imaging Techniques

TODO:

Time Difference

Frequency Difference

Absolute

2.1.7.1 Absolute

Imaging the absolute difference in tissue impedance is challenging due to the non-linear trajectory of electrical current, individual anatomy and difference in electrode

contact impedance.

2.1.7.2 Frequency Difference

2.1.7.3 Time Difference

Time difference EIT uses a reference frame to image the change in conductivity between two points in time and allows for imaging of functional activity such as the inflation of the lungs and the flow of blood.

2.2 Lung perfusion monitoring

2.2.1 Sensitivity to Blood Movement

2.2.2 Contrast agent injection

2.2.3 Frequency Filtering

Monitoring lung ventilation is one of the most established clinical uses of EIT, presented initially by Barber and Brown (**Barber1984**). EIT has also been used as a tool to monitor blood perfusion (**Brown1992**) and hemodynamic parameters such as cardiac output (**Braun2018**) and blood pressure (**Sola2011; Proenca2017**). While the spatial resolution of EIT is much lower than intermittent imaging techniques such as computed tomography (CT) or magnetic resonance imaging (MRI), EIT can have a high temporal resolution enabling continuous or frequent monitoring without concerns regarding radiation exposure. This thesis focuses on time difference

EIT for thoracic hemodynamic imaging and monitoring applications.

EIT is sensitive to the movement of blood in two main ways. First, a conductivity-contrasting bolus solution injected into a vein or artery can be used to image the transit of blood through the body and second, the pulsatile changes in conductivity at the cardiac frequency can be isolated through digital filtering (**Leathard1994**). This document proposes methods and techniques to identify and isolate these impedance variations to monitor lung perfusion and aortic flow.

A perfusion scan is a technique for imaging the blood flow through the lungs and when compared with ventilation images can be used to detect pulmonary embolisms when a mismatch is identified. Clinically pulmonary perfusion is done using lung nuclear medical imaging such as single photon emission computed tomography (SPECT) (**Parker2012**). Radio-isotopes are inhaled through a mask for ventilation imaging and injected into the blood to image pulmonary perfusion. Images taken on a gamma camera are compared to look for a mismatch between the ventilation and perfusion distribution. This method of measuring lung perfusion is slow and exposes the subject to low-dose radiation.

EIT has been evaluated for its ability to measure cardiac output and lung perfusion since the late 1980s (**Eyuboglu1989; Blottt1992; Brown1992; Frerichs2002**). Since then, various configurations of EIT have been evaluated (**Borges2012; Nguyen2015**). Due to the speed and safety of measurement acquisition, EIT might be used to continuously monitor perfusion in subjects.

There are two main challenges with perfusion monitoring using EIT. First, impedance change due to ventilation is 10 times larger than the impedance change

due to cardiac-frequency pulsatile activity (**Deibebe2008**) and second, the pulsatile activity outside the lung region can overwhelm the lung perfusion signal (**Stowe2019**). There are several techniques available to mitigate the difference in magnitude such as: pausing ventilation; administering a conductivity-contrasting bolus through the heart and lungs via the jugular (**Frerichs2002**); and digital filtering to isolate activity at the cardiac frequency (**Leathard1994**).

When breathing is paused, the signals based only on the cardiac activity can be more easily extracted. It was found that during apnoea the global impedance recorded with EIT measurements corresponded with stroke volume measured using the thermodilution method with a pulmonary arterial catheter (**Fagerberg2009**). Ventilation perfusion ratios have been calculated during apnoea by comparing ventilation and perfusion signal amplitude with a specified region of interest (**Fagerberg2009a**). There is some concern that the perfusion measured during apnoea may not accurately represent true perfusion during regular respiration as the apnoea impacts the regular respiratory cycle (**Leonhardt2012**).

Using the conductivity-contrasting bolus injection EIT perfusion imaging has been compared to SPECT measurements, and blood flow has been imaged from the right heart into the lungs and back into the left heart using 5-10% hypertonic saline (**Frerichs2002; Borges2012**). This technique is promising for imaging lung perfusion, but is slow and requires the placement of a venous catheter and repeated saline injections to obtain perfusion measures.

The final method to calculate perfusion using EIT is through filtering to isolate the cardiac related signal. Previous work has shown that principal component

analysis (PCA) can be used to separate ventilation and cardiac frequency signals and identify the component related to the heart (**Deibele2008**). Once the cardiac-frequency component of the EIT signal is identified the pulmonary component must also be isolated. Other than visual identification of the lung region or manually selecting a region of interest, there are few good solutions for isolating pulsatile activity within the lung region.

The use of 3D configurations to differentiation between pulsatile activity in the heart and lungs could allow for an improved perfusion measure using EIT, and a means of continuously monitoring perfusion during ventilation.

2.3 Aortic flow monitoring

Continuous bedside monitoring appears to be one of the most promising future applications of EIT due to the high temporal resolution, and concerns with other imaging modalities and the associated radiation exposure.

Another potential use of EIT is to replace invasive monitoring techniques such as catheterized measurements of pulmonary arterial pressure. Recent studies have evaluated EIT as a method of determining pulmonary arterial pressure using pulse wave velocity in the descending aorta in 2D (**Braun2018a; Proenca2017; Proenca2016**). EIT was used in conjunction with ECG signals and shown to have a high correlation with pulmonary arterial pressure values from Doppler echocardiography (**Proenca2016**).

An analysis of hemodynamic measures using EIT found that measures of stroke

volume and pulmonary arterial pressure are sensitive to electrode placement and interference from pulmonary signals (**Braun2018a**). The solution proposed in this document uses an arrangement of internal electrodes placed in the esophagus adjacent to the aorta to increase the sensitivity to changes and improve detection accuracy and elimination of pulmonary signals.

Improving tracking and imaging of the aorta is also important because it has additional clinical uses: it can be used as a physiological landmark to identify the back of the lungs, and can be used to continuously monitor blood pressure by calculating the pulse transit time.

EIT has been used clinically to monitor lung perfusion in an animal model (**Leonhardt2012; Nguyen2012**), and it is theorized that the use of an internal electrode for increased sensitivity may allow for imaging of blood flow in the aorta. There is great interest in monitoring cardiac parameters using EIT to determine stroke volume (SV) (**Proenca2017; Braun2018**), and increased sensitivity close to the heart also has the potential to improve these measures.

While there have been some studies researching electrode placement for cardiac imaging in 2D (**Noordegraaf1996**) and 3D electrode configurations (**Graham2007**), there has been little research into determining the optimal 3D external electrode configurations for imaging the heart and aorta.

Additionally when using alternate electrode configurations the current injection and measurement patterns must also be investigated. It has been suggested that an internal electrode in 2D should not be used for current injection in asymmetrical models as the reconstruction performance deteriorates (**NasehiTehrani2012**). It is

unclear to what degree injection patterns affect the resulting sensitivity when internal electrodes and alternate electrode arrangements are used in 3D.

This work aims to investigate internal and external electrode configurations for use in imaging blood movement in the thorax, and develop techniques to extract measures of aortic flow and lung perfusion from these reconstructions.

Chapter 3

Comparison of bolus- and filtering-based EIT measures of lung perfusion in an animal model

3.1 Summary

Objective: Two main functional imaging approaches have been used to measure regional lung perfusion using Electrical Impedance Tomography (EIT): venous injection of a hypertonic saline contrast agent and imaging of its passage through the heart and lungs, and digital filtering of heart-frequency impedance changes over sequences of EIT images. This paper systematically compares filtering-based perfusion estimates and bolus injection methods to determine to which degree they are related.

Approach: EIT data was recorded on 7 mechanically ventilated newborn lambs in

which ventilation distribution was varied through changes in posture between prone, supine, left- and right-lateral positions. Perfusion images were calculated using frequency filtering and ensemble averaging during both ventilation and apnoea time segments for each posture to compare against contrast agent-based methods using Jaccard distance score. *Main Results:* Using bolus-based EIT measures of lung perfusion as the reference frequency filtering techniques performed better than ensemble averaging and both techniques performed equally well across apnoea and ventilation data segments. *Significance:* Our results indicate the potential for use of filtering-based EIT measures of heart-frequency activity as a non-invasive proxy for contrast agent injection-based measures of lung perfusion.

3.2 Introduction

Electrical Impedance Tomography (EIT) uses electrical stimulation and measurements at electrodes on the body surface to reconstruct images of internal conductivity distribution and its changes. The most common application of EIT, experimentally and clinically, has been for imaging of the thorax (Frerichs *et al.*, 2017). Using a ring of electrodes around the chest, EIT is able to calculate images of impedance changes in the abdomen. Although most research has focused on imaging of ventilation, there is significant interest in imaging cardiovascular phenomena with EIT (Adler *et al.*, 2012; Leonhardt and Lachmann, 2012).

EIT has been evaluated for its ability to measure cardiac output and lung perfusion since the early 90s (Eyüboğlu *et al.*, 1989; Frerichs *et al.*, 2002; Zadehkoochak

et al., 1992). Since then, various configurations of EIT have been evaluated (Borges *et al.*, 2012; Nguyen *et al.*, 2015). The effect of posture on EIT images was evaluated by Reifferscheid *et al.* (2011), who showed that changing posture introduces a large and reproducible variability into ventilation distribution as imaged by EIT. Based on results showing a common relationship between the effect of gravity and perfusion in both children and adults (Bhuyan *et al.*, 1989), in newborns we expect to see a comparable directional change in perfusion due to the changes in posture. Recently, Braun *et al.* (2018) evaluated EIT’s ability to monitor cardiac output, showing that EIT is more reliable for monitoring cardiac output trends than absolute cardiac output. EIT has also been investigated for monitoring of systemic blood pressure (Solà *et al.*, 2011), and for monitoring of pulmonary arterial pressure (Proença *et al.*, 2017).

EIT measurements are sensitive to blood movement in two main ways. First, it is possible to image the transit of the contrast agent through the heart and lungs via a conductivity-contrasting bolus into the veins and second, through digital filtering of the time series of EIT images at the heart frequency (Leathard *et al.*, 1994). While multiple EIT measures of perfusion are used, their relationship is not well understood. It is currently unclear to what degree pulsatile impedance changes represent blood flow, and how they limit the potential for heart-frequency filtering to correctly estimate the true perfusion (Nguyen *et al.*, 2012).

Injection of a contrast agent to measure regional lung perfusion has been compared with electron beam computed tomography (EBCT) and determined to be feasible for measuring perfusion across different animals (Frerichs *et al.*, 2002). Perfusion measurement via conductivity contrasts has the advantage of measuring the

true perfusion, but requires placement of a catheter to introduce the contrast agent. Bolus-derived measurements cannot be made continuously because they rely upon the circulation of a contrast agent. In addition, the accumulation of NaCl (the main conductivity contrast used) over multiple injections can lead to hypernatremia which limits the rate at which bolus injections can be made.

Calculating the heart-frequency conductivity changes in the thorax offers the benefit of a continuous functional measure calculated directly from EIT signals (possibly in conjunction with a synchronization signal such as the ECG). Heart-frequency EIT signals are typically an order of magnitude smaller than ventilation signals; thus, when measurements are made during tidal ventilation, a large period of data must be used in order to reduce the ventilation signal. On the other hand, measurements during apnoea can be used to eliminate the ventilation signal, but for the safety of the patient the apnoea was limited to 30 s. In healthy human subject of less than one year old it takes a mean of 118 s for the blood oxygen saturation levels to drop below 90% (Fu *et al.*, 1996), however the length of safe apnoea is much shorter for the sick preterm infant. The time period was chosen based on experience in the lab showing that 30 s seconds was not associated with bradycardia or desaturation to less than 90% blood oxygen saturation.

There is a debate within the EIT community about the meaning of heart-frequency EIT signals (Adler and Boyle, 2017; Frerichs *et al.*, 2017). Not all perfusion results in a cardiac-frequency change (for example, continuous blood flow in capillaries), and non-perfusion effects (for example, heart movement in the thoracic cavity) can result in heart-frequency EIT signals. This debate is reflected by the terminol-

ogy – perfusion vs. pulsatility. Those who prefer “pulsatility” or “heart-frequency fEIT image” seek to emphasise that frequency filtered signals are not “perfusion” (although they may be related). While these pulsatility based EIT images are clearly not a direct measure of perfusion, the signals appear to be useful and are often measured and reported (Bartocci *et al.*, 1999; Ericsson *et al.*, 2016; Halter *et al.*, 2008; Moens *et al.*, 2014). To the authors’ knowledge, no systematic comparison of frequency-based perfusion measures has been published.

The heart-frequency signal can be derived from frequency filtering or ensemble averaging. Frequency-filtering uses a filter to isolate the frequency of heart-frequency conductivity changes, and was introduced by Zadehkoochak *et al.* (1992) and Leathard *et al.* (1994). Frequency filtering is susceptible to interference from ventilation when the heart rate is at a harmonic of the breathing rate. Ensemble averaging is another filtering approach which averages signals at a synchronized time, for example at the QRS peak (Bartocci *et al.*, 1999; Deibele *et al.*, 2008). The impedance change due to each heart beat is aligned and averaged to give a single heart-related impedance change, representative of all heart-beats in the segment.

In this paper, we are motivated to better understand the relationship between lung perfusion and heart-frequency filtering measures, and between the various filtering approaches used to determine heart-frequency components. Our questions are: 1) to what extent do heart-frequency filtering-based measures correspond to perfusion, 2) what are the advantages and disadvantages of different approaches to heart-frequency filtering of EIT data, and 3) which techniques are recommended. In our experimental protocol, we have selected posture-change to introduce changes in

the regional distribution of lung perfusion. These changes are then compared using bolus- and filtering-based EIT measures.

3.3 Methods

3.3.1 Overview

Data were acquired as an additional protocol within a study to determine a baseline for lung damage due to gas ventilation in neonatal lambs. This is part of an effort to establish total liquid ventilation (TLV) as a less-injurious ventilation strategy for the delicate lungs of neonatal subjects (Sage *et al.*, 2018). In order to induce changes in ventilation and perfusion patterns, posture changes were made between supine, prone, left and right lateral positions.

3.3.2 Animals

The study was conducted in accordance with the Canadian Council on Animal Care guidelines upon approval by the animal research ethics board of Université de Sherbrooke (protocol 417-17BR).

Seven healthy neonatal lambs (2–4 days old and 2.95 ± 0.27 kg) were used. Animals were anaesthetised (ketamin 10 mg/kg IM at induction followed by propofol 100 mcg/kg/min and ketamin 2 mg/kg/h IV) and placed under mechanical gas ventilation with: peak inspiratory pressure (PIP) 15 cmH₂O, positive end-expiratory pressure (PEEP) 5 cmH₂O, respiratory rate (RR) of 60/min, and fractional concentration of O₂ in inspired gas (FiO₂) of 30%.

A catheter was inserted into the carotid artery for blood gas and continuous blood pressure monitoring. A jugular venous access was inserted to inject the saline bolus for generating perfusion images. Each animal was shaved for placement of a custom EIT belt around the lower third of the sternum in the transverse plane.

For each animal a bolus injection protocol was used: 1.5 mL of 7.5% saline was injected into the jugular vein at a constant rate over approximately 2s. Before each bolus, ventilation was stopped for ten seconds, and a further twenty seconds of apnoea was maintained before restarting ventilation.

After one hour of ventilation (for stabilization) EIT recordings were made during the position change procedure. Each lamb was rotated onto its right side. Five minutes after turning the subject, the bolus injection protocol was implemented. The animal was then ventilated normally, remaining on the right side for an additional five minutes, before being positioned on the left side for 5 minutes of regular ventilation, followed by the bolus injection protocol.

At 2 hours of ventilation, the position change procedure was repeated, changing the positioning of the lamb from prone to supine as the bolus injection protocol was repeated and EIT recordings were captured.

3.3.3 Data Acquisition and Image Reconstruction

EIT data was acquired with the Pioneer Set (Swisstom, Landquart, Switzerland) using a custom electrode belt (at an acquisition rate of 20 frames/s). The belt uses 32 brass electrodes equally spaced around the thorax, using an ultrasound gel to ensure good contact and minimise the contact impedance. The selected data in

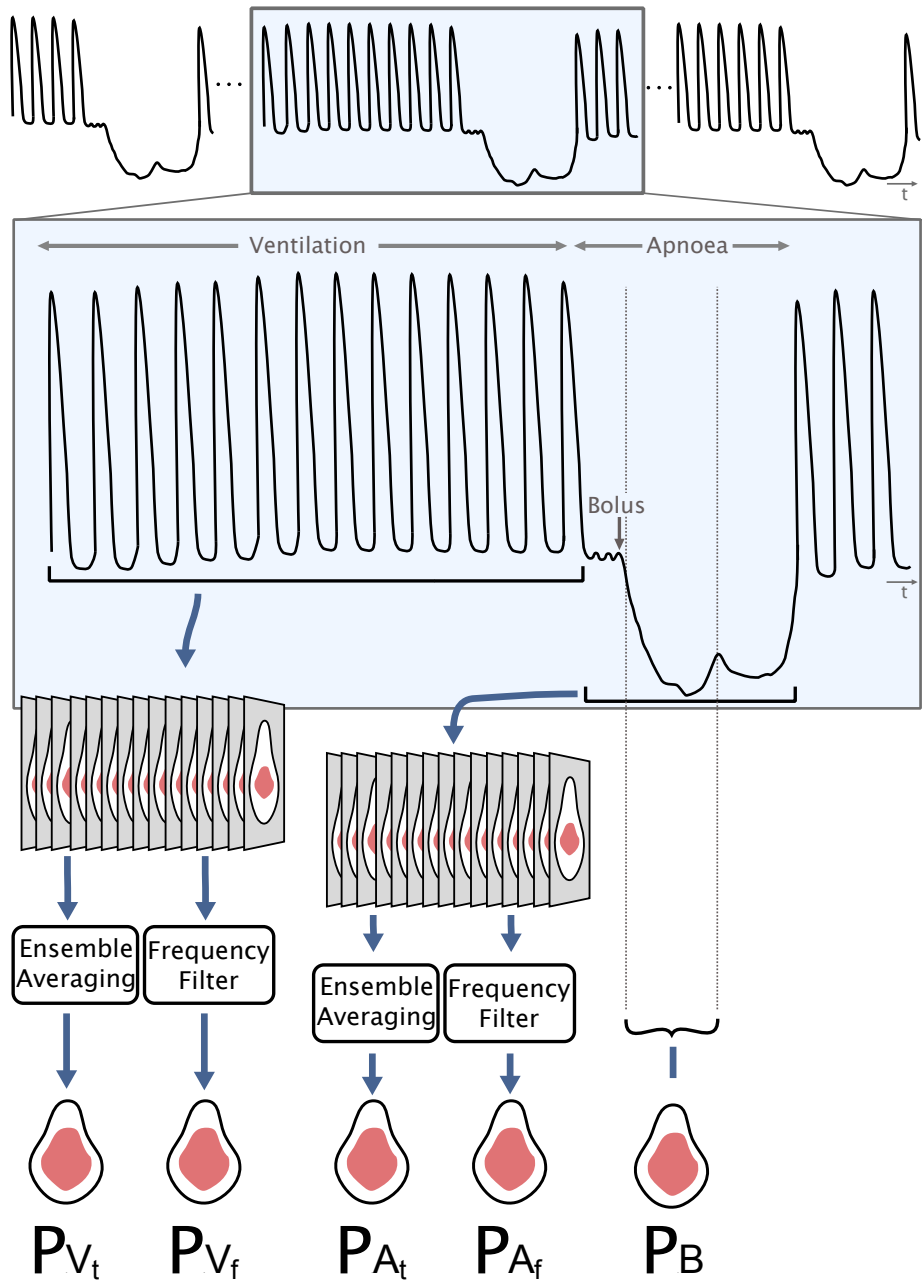


Figure 3.1: This figure is a schematic overview of analysis methods for EIT perfusion. The upper curve illustrates the global EIT signal during a period of ventilation followed by apnoea and renewed ventilation. During apnoea a bolus of conductivity contrasting saline is introduced. From these data 5 fEIT images are calculated: P_{Vt} : pulsatility (perfusion) image during ventilation, calculated by ensemble averaging EIT data during ventilation; P_{Vf} : pulsatility (perfusion) image during ventilation, calculated by frequency filtering EIT data during ventilation; P_{At} : pulsatility (perfusion) image during apnoea, calculated by ensemble averaging EIT data during apnoea; P_{Af} : pulsatility (perfusion) image during apnoea, calculated by frequency filtering EIT data during apnoea; P_B : perfusion image from bolus, calculated between a reference measure during apnoea and one during the bolus

this study comes from lateral positioning changes recorded after 1.5 hours of ventilation and prone to supine positioning changes after 2 hours.

EIT images were reconstructed using GREIT (Adler *et al.*, 2009), which calculates a reconstruction matrix \mathbf{R} from which the reconstructed image is calculated as $\hat{\mathbf{x}} = \mathbf{R}\mathbf{y}$, where \mathbf{y} are the time-difference measurements, $\mathbf{y}(t) = \mathbf{v}(t) - \mathbf{v}(t_r)$, where $\mathbf{v}(t)$ represents the data frame acquired at time, t , and $\mathbf{v}(t_r)$ measurements acquired at a “reference” time, t_r in the case of this experiment the reference was a mean of 10 images preceding the bolus injection.

The linear reconstruction matrix $\mathbf{R} = \mathbf{D}\boldsymbol{\Sigma}_t\mathbf{J}^T(\mathbf{J}\boldsymbol{\Sigma}_t\mathbf{J} + \boldsymbol{\Sigma}_n)^{-1}$ is calculated from a finite element model of the body and electrode geometry $F(\cdot)$ and covariance estimates of the image, $\boldsymbol{\Sigma}_t$, noise, $\boldsymbol{\Sigma}_n$ (Grychtol *et al.*, 2016), and a spatial filtering matrix, \mathbf{D} .

EIT data from this experiment was prone to errors consisting of brief periods of zeroed measurements stemming from the synchronisation equipment. Measurements that were zeroed by the device were removed and replaced with linearly extrapolated data to allow for frequency-based analysis over all selected segments of data. A moving median filter with a width of 3 was used to further remove the noise caused by single measurement errors in the signal.

3.3.4 Functional EIT Images

In each animal 4 episodes were recorded — one in each posture — to generate 5 different functional EIT images.

The images Bolus-based measures of lung perfusion (P_B) were calculated using

time-difference reconstructions. Heart-frequency filtering during ventilation (P_{Vf}) and apnoea (P_{Af}) used frequency analysis of EIT image sequences, as illustrated in figure 3.3 on page 25, and ensemble averaging-based methods during ventilation P_{Vt} and apnoea P_{At} are calculated using ensemble averaging of identified pulsatile components figure 3.4 on page 26.

The following methods were conducted on segments of data collected both during apnoea and ventilation. Apnoea regions were selected as the total time that ventilation was arrested, including the bolus section and had a duration of 30s. The ventilation data was selected as 30s of data immediately preceding the induction of apnoea. Regions of interest including lung, and heart areas in the images were defined by the lamb model provided in EIDORS (Adler *et al.*, 2017).

3.3.4.1 Bolus injection image (P_B)

The beginning of the saline bolus injection was determined as the point immediately preceding the drop in impedance from the conductive agent, and is shown in figure 3.2 on the next page at the point marked “injection”. The mean of 10 images including and immediately preceding the bolus injection were used as the reference to which all bolus images were reconstructed from. To image perfusion, the point with maximum decline in impedance over the sum of the pixels in the lung region relative to the reference was selected based on the methods presented by Frerichs *et al.* (2002). In figure 3.2 on the following page this was found at the point marked “perfusion”. This method was used as the standard perfusion measuring technique against which the other methods were compared.

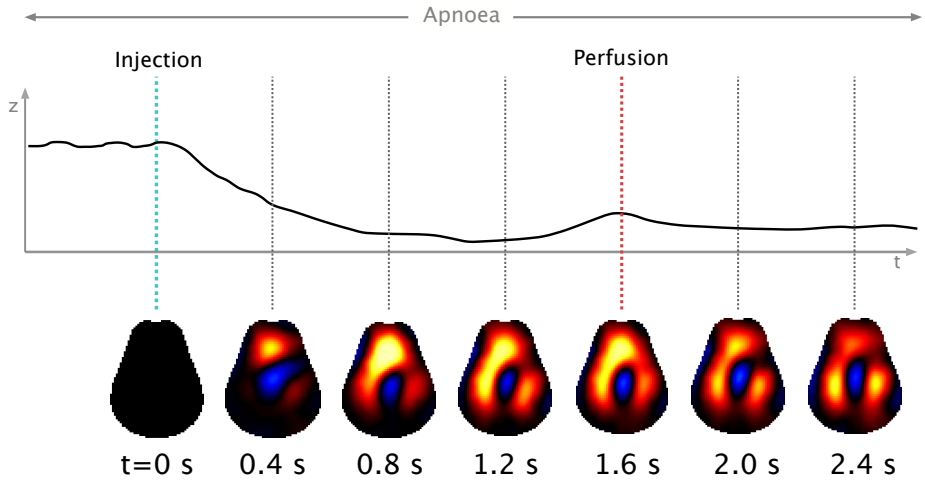


Figure 3.2: The method used to select the perfusion point from the bolus injection is shown in the figure above. The point with the widest spread of high conductivity was selected as the point of perfusion, shown here at 1.6 seconds after the contrast agent injection. The image series shows the conductivity contrast as the bolus injection travels through the thorax.

3.3.4.2 Frequency-Filtering

Heart-frequency EIT images during the selected events were calculated by taking the FFT of the time-series image data after first applying a Blackman window: $w(n) = a_0 - a_1 \cos\left(\frac{2\pi n}{N-1}\right) + a_2 \cos\left(\frac{4\pi n}{N-1}\right)$ with $a_0 = 0.42$, $a_1 = 0.5$ and $a_2 = 0.08$, where N is the number of time-series EIT images in the selected event.

An FFT was calculated from a series of images restricted to pixels in the heart region. From the FFT of all pixels the heart region, the heart frequency was selected as the largest peak between 3 and 4.5 Hz, representing a heart rate between 180 and 240 bpm (typical for a newborn lamb).

The identified heart rate was used to select changes at the heart-frequency in the frequency domain images of the entire thorax. Images at 3 frequencies on either

side of the heart rate were also reconstructed to account for changes in heart rate over the course of the data collection. A Blackman window with a length of 7 was applied surrounding the heart frequency to generate a weighted mean of the images, resulting in a single perfusion image from the heart-frequency data.

The output of the frequency filtering method is an image with complex values assigned to each pixel.

Depending on the timing of the pulsatility-based changes within the selected signal the real component of frequency analysed image did not correspond to the maximum conductivity change in the lungs in every event. In order to correct this, each image was displayed along the axis that gave the maximum real component contained within the lung region to ensure the maximum change in impedance related to pulsatile activity in the lungs was calculated.

3.3.4.3 Ensemble Averaging

Time series data of the total impedance signal for each pixel in the heart region was filtered using a bandpass filter to eliminate noise and breathing changes, and allow the heartbeat to be seen clearly in the signal. Peak detection was used on this heart-region data to select the amplitude peaks in impedance change signal at the heart frequency.

Using the identified time points, the global impedance change signal was ensemble averaged by overlaying all identified peaks to give an averaged heartbeat. 13 images were reconstructed over the course of the heart beat to select the image that resulted in the maximum positive increase impedance within the lung region. This process is

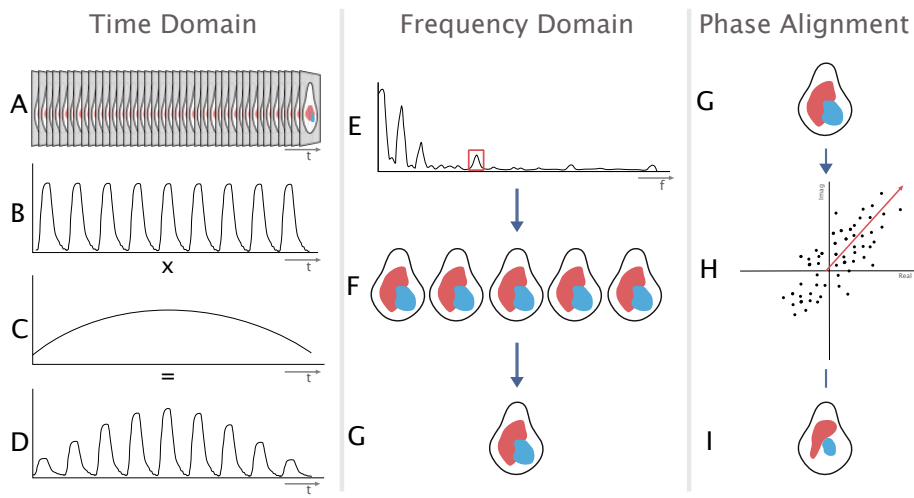


Figure 3.3: Frequency analysis methodology used for obtaining a perfusion image from the time series data. Steps are: A) to reconstruct the images from time series measurements; B) - D) window the time series data before performing a FFT on the data for each element; E) Select the dominant frequency between 3 and 4.5 Hz as the heart frequency; F) reconstruct the image at the heart frequency and selected nearby frequencies; G) take the mean of the images at the heart frequency using a Blackman window to give greater weight to those closer to the center; H) I) select the image that will give the maximum real component contained in the lung region.

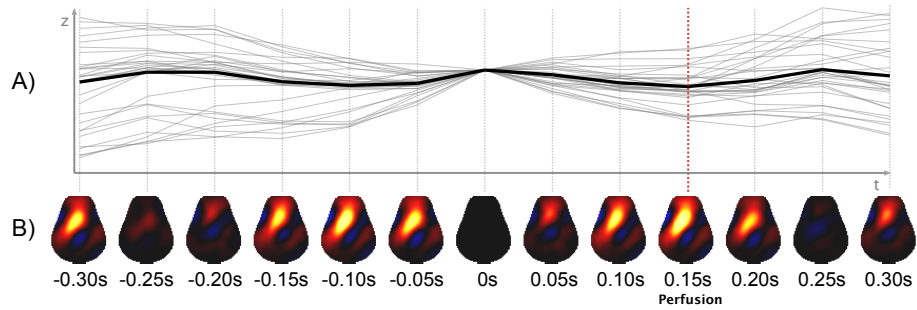


Figure 3.4: Illustration of the stages of the ensemble averaging process: A) an ensemble average of all heartbeats over the time frame is taken from the summed global signal; and B) shows reconstructed images corresponding to each time point in the global ensemble averaged signal above. The selected perfusion image is the image with the maximum impedance increase in the lung region.

outlined in figure 3.4.

3.3.5 Image Comparison

To compare the images the Jaccard distance between functional EIT images was calculated. Negative impedance changes were removed from the images and the images were normalized.

The Jaccard distance was calculated between the reference image calculated using the maximum increase in lung-region conductivity during bolus injection (b), and the frequency-based method (f): $J(x, y) = \sum_i \frac{\min(b_i, f_i)}{\max(b_i, f_i)}$ representing the distance between the two images.

3.3.6 Statistical Analysis

To determine the significance of the change in bolus between postures and methods, the Cohen's d score was calculated to quantify the effect size of the change in the centre of mass of the perfusion image (Cohen, 1977). This was calculated as the difference between two means over the pooled standard deviation. Where the difference between the two means is: $\mu_1 - \mu_2$, and the pooled standard deviation is:

$$\sqrt{\frac{(n_1-1)s_1^2 + (n_2-1)s_2^2}{n_1+n_2-2}}.$$

3.4 Results

The Jaccard scores for each method were compared between ensemble averaging and frequency filtering methods to determine the regions where performance was best for each method. Figure 3.5 shows a comparison between Jaccard distance for each animal, connecting lines indicate different methods performed on the same data segment, while each marker shape denotes a separate posture.

On average frequency filtering outperforms ensemble averaging based methods of perfusion calculation ($p=0.04$), and there is no significant difference in performance of the heart-frequency based filtering techniques during periods of apnoea relative to periods of ventilation.

Of the 56 data regions that were analysed, the ensemble averaging performed better in 12 cases and the frequency filtering achieved the best performance in 28 cases, there, were 16 additional cases where the difference in performance was negligible at less than 5%. On average, across all images, frequency filtering based methods

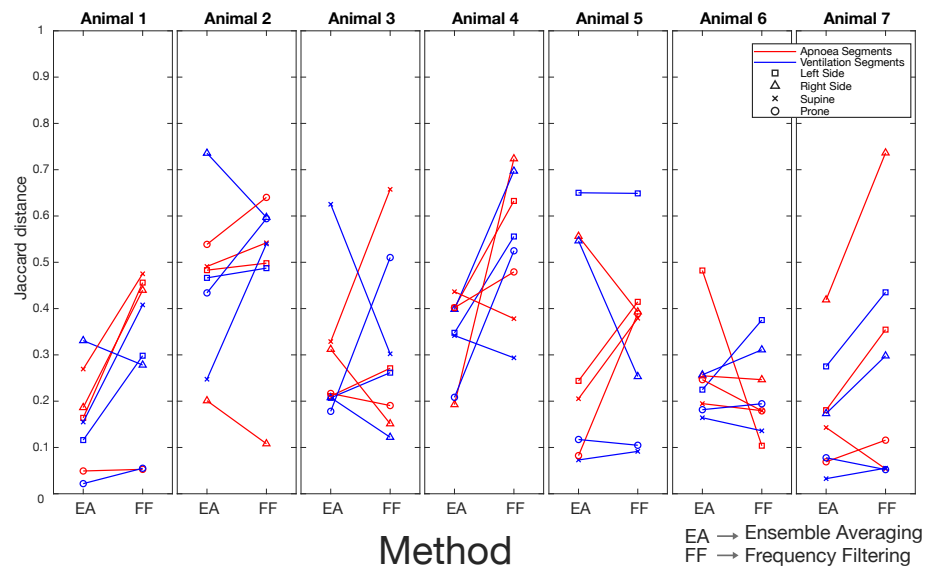


Figure 3.5: Jaccard scores for each method and animal in the comparison. Frequency filtering and ensemble averaging methods performed on the same data segment are connected by solid lines. Red lines and markers indicate apnoea data sections, while blue indicates ventilation data sections. Each posture is denoted by a different shaped marker in the figure.

scored 7% higher than ensemble averaging.

The center of mass of the perfusion measure images using the bolus injection method had a Cohen's d score of less than 0.1 between posture changes indicating that there is an insignificant or trivial difference in the means relative to the standard deviation (Cohen, 1977). To demonstrate the visually observable changes due to posture change and the high similarities that can be observed between filtering- and bolus-based perfusion estimates, frequency filtered images from animal 4 are compared to bolus based methods in figure 3.6 on the following page.

3.5 Discussion

Two primary approaches of EIT perfusion calculation have been compared in this paper: injection of a bolus of contrast-agent resulting in EIT image changes which produce perfusion measures, and digital filtering of EIT image sequences to extract the heart-frequency components. Additionally, various algorithms have been evaluated for digital filtering-base approaches during mechanical ventilation and short apnoea sequences, using both frequency- and ensemble averaging-based techniques. There have been few comparisons of these techniques, and we set out to better understand the relationship between perfusion and heart-frequency measures, and between the various filtering approaches used to determine heart-frequency cardiac changes. We selected an experimental protocol using posture-change to alter the regional distribution of lung ventilation and perfusion in newborn lambs.

Our first question was “to what extent do heart-frequency filtering-based mea-

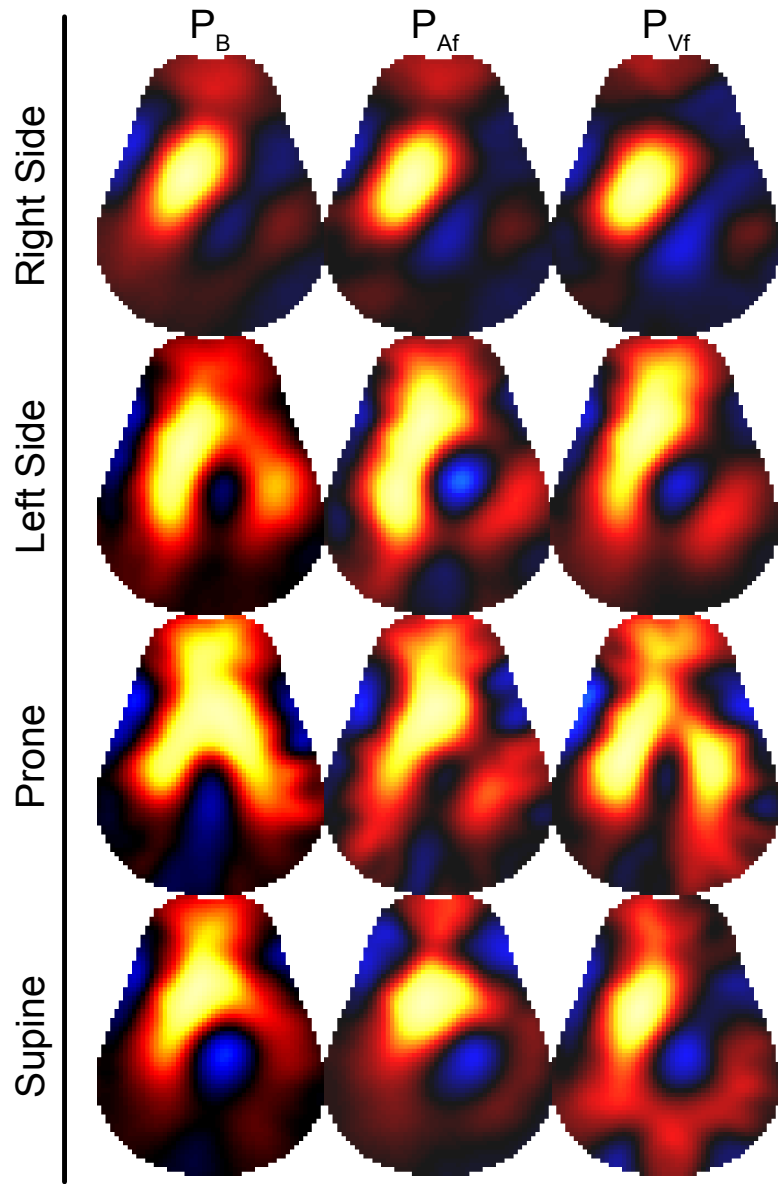


Figure 3.6: This figure shows the tracking of perfusion for frequency filtering measures of perfusion during apnoea and ventilation sections compared to bolus injection for animal 4. P_B is the bolus injection image, P_{Af} uses the frequency filtering method during apnoea and P_{Vf} is the frequency filtering method during ventilation.

sures correspond to perfusion?"

The primary results (figure 3.5 on page 28) use a Jaccard index of the similarity between functional images. Overall it was found that in healthy animals the Jaccard index indicated good agreement with our gold standard. While highly dependant on the data, it was found that there was a high degree of similarity between methods with respect to the overall shape of the perfusion. In both animals 2 and 4, where the signal required little preprocessing before analysis there is a higher Jaccard score across all cases.

The synchronisation box was attached to the EIT system but was not used for this experiment, an error in the connection caused brief periods of the signal (less than 1 s) in some animals to be zeroed. Through careful processing of this signal only brief sections of data were lost and we do not feel this impacts the results.

During the experiment the order of posture change was not randomised. While changes in ventilation due to posture change are not understood to have long term physiological effects, if there is a longer term effect of change in posture the lack of randomisation will impact the results. Nguyen *et al.* (2015) were able to image perfusion changes due to induced pulmonary embolisms and using the peak impedance change on dilution curves, however our data presented insufficient variance in perfusion induced by posture change to complete a center of mass analysis. A higher statistical power could potentially be achieved through initiating posture changes with more dramatic results in perfusion, such as upright to supine (Nakazato *et al.*, 2010).

Throughout the experiment, the perfusion image was selected as the image con-

taining the largest increase in conductivity in the sum of pixels in the lung region, which occurred at different relative times across animals and events. Many factors could affect this including belt positioning changes, and it could be a contributing factor to the inconsistent trends in amplitude changes in the global image across methods. Borges *et al.* (2012) compared EIT perfusion images using first-pass kinetics and heart-frequency filtering based methods to perfusion measures using SPECT, finding that heart-frequency filtering techniques made systemic errors when used to estimate the perfusion. They also determined that there was no discernible relationship between the magnitude of the SPECT images and the heart-frequency images. This was consistent with the findings of this study that image amplitude of the bolus injection and heart-frequency filtering-based methods was not consistent in all animals. This methodology presented by Borges *et al.* (2012) was not part of the comparison in this study as the edentification of the perfusion signal due to the heart could not be consistently identified and removed across all animals. In two dimensions, heart-frequency and ventilation signals have been used to identify the location of the heart and lungs within the EIT electrode plane with known electrode locations and anatomy (Ferrario *et al.*, 2012), but in situations where the electrode location and anatomy is not precisely known EIT tends to perform poorly as a structural imaging modality (Adler and Boyle, 2017). These challenges suggest that configurations with multiple planes of electrodes may be better able to isolate and remove off-plane pulsatility signals related to the heart.

It was observed that the general shape of the perfusion was consistent across all methods despite amplitude variations. One reason for the difference in amplitude

change across animals may be due to slight variations in the belt placement and electrode positioning on the animals. If the belt is closer to the heart, there will be a larger heart-frequency component to the signal and there may be a variance in the impedance change due to bolus injection.

Next, we asked “what are the advantages and disadvantages of different approaches to heart-frequency filtering of EIT data, and which techniques are recommended under which circumstances?”

Our overall recommendation is that, whenever possible, frequency filtering techniques should be used. This is largely because frequency filtering methods tend to be more stable in the presence of noise on the signal. Ensemble techniques are advantageous in some circumstances, because they better use the heart-frequency variability to avoid interference from harmonics of the ventilation at the heart rate. For frequency-filtering techniques, it is necessary to widen the heart-frequency filters to account for such variability. On the other hand, it is sometimes not possible to accurately synchronize heartbeats, due to noise corruption in the signals or the very low amplitude of the heart-frequency signals relative to the ventilation signal. In cases where the signal of the heartbeat was not clearly identifiable through visual inspection of the signal, neither ensemble averaging nor frequency filtering was able to achieve good estimates of perfusion relative to the bolus injection event.

In summary, our goal was to understand the relationship between bolus- and filtering-based EIT measurements of lung perfusion, as well as the relationship between different filtering-based measures of perfusion. Our results indicate there is a common trend between the shape and perfusion estimates of both heart-frequency

and bolus injection images despite the difference in physiological events behind each measure. Amongst filtering techniques, frequency filtering outperforms ensemble averaging across regions of data where there is noise present and the heart signal cannot be readily identified, and both methods were able to approximate the bolus injection measures equally well when applied to apnoea and ventilation regions of data.

Chapter 4

FEM mesh refinement for 3D Electrical Impedance Tomography

4.1 Summary

In this paper we examine the requirement for mesh refinement around electrodes in Electrical Impedance Tomography (EIT). While it has been recommended that models be refined around the electrodes, where current density and sensitivity are highest, the level of refinement required is poorly understood. Using a set number of nodes, we investigate the optimal distribution between the electrodes and the volume of a model. A balance point is used to measure the difference in distribution between the electrode and the centre of the model. To calculate this, all nodes contained between the surface of a selected electrode and the centre of the model were identified and the mean position of nodes along the container axis was computed.

We compare refinement strategies across commonly used meshing software in EIT and compare the model sensitivity error to an ultra-fine reference mesh. In a tank model, for a fixed number of nodes, error in the sensitivity calculation is minimized when the balance point of the nodes is at 85% of the tank radius and the node density dissipates evenly from the electrode surface to the centre of the model. Using this method sensitivity error was decreased in all regions with high sensitivity. This node distribution technique enables the generation of accurate meshes with fewer nodes that can reduce measurement error and computing time.

4.2 Introduction

Electrical Impedance Tomography (EIT) reconstructs images of electrical tissue properties within a body from electrical transfer impedance measurements at surface electrodes. For biomedical imaging applications, it is being actively studied for monitoring the movement of air and blood in the thorax, and for imaging the head and breast. Reconstruction of EIT images requires the solution of an inverse problem in soft field tomography. EIT image reconstruction requires calculation of a sensitivity matrix, \mathbf{J} , representing the relationship between internal changes and measurements. A pseudo-inverse of \mathbf{J} is used to update the image estimate over several iterations. EIT image reconstruction is ill-posed, since the physics of current propagation implies that sensitivity is largest near the electrodes and smallest in the body centre.

It is therefore clear that a precise calculation of \mathbf{J} is required for solution accuracy. Since it is generally not possible to use analytic solutions, because of the non-regular

shapes of biological bodies and the boundary conditions on a conductive electrode, the finite element method (FEM) is typically used. One key advantage of the FEM is that element size can be selectively refined in regions to meet solution accuracy. The accuracy of the FEM solution will increase as more elements are added, so a high mesh density is often desired to achieve an accurate solution. In this paper we will use the term mesh to refer to a specific combination of nodes and elements in a finite element model. In EIT the sensitivity is nonuniform across the entire model. Thus it has generally been recommended in the EIT literature that meshes be refined near electrodes, where the electric field and sensitivity are largest (Adler and Boyle, 2017). This recommendation gives rise to two questions: 1) No thorough analysis has been made to determine how much refinement is required. Given a “mesh element budget”, what should balance of nodes be between the centre of the model and the electrodes? And 2) How do different freely available meshing tools that are commonly used with EIT compare when used to refine 3D meshes?

Previously with EIT, mesh refinement has primarily been either constant, or based on the complexity of geometric surfaces and lines within a model (Grychtol and Adler, 2013). In EIDORS (Adler and Lionheart, 2006) meshes are generated using both Netgen (Schöberl, 1997) and Gmsh (Geuzaine and Remacle, 2009) for 2D and 3D models. Refinement around electrodes is commonly performed by setting a mesh density for the electrodes and allowing the mesh density to decay towards the maximum mesh size. This does not allow the user to specify the rate of decay or precisely control the mesh size.

A model that accurately represents the anatomy of the imaged region can greatly

increase the quality of the reconstructed image (Grychtol *et al.*, 2012), but increasing the complexity of mesh surfaces presents additional challenges for mesh refinement. EIT reconstruction software EIDORS enables users to place electrodes on the surface of complex boundaries (Grychtol and Adler, 2013), but the current functionality does not enable control of the refinement around the electrodes or internal structures. Most commercially available FEM packages do not conveniently provide such capability either.

In this paper we investigate approaches to manage the tradeoff between refinement of the electrode regions versus the bulk volume. We present a comparison between Gmsh and Netgen based mesh refinement around electrodes, and evaluate the effect of mesh refinement techniques on error in the sensitivity matrix, \mathbf{J} .

4.3 METHODS

4.3.1 Overview

We built a cylindrical model in Gmsh and Netgen which was parameterized so that multiple different combinations of mesh refinement were possible. These results were compared to a very high density meshes which was considered the gold standard.

4.3.2 Mesh Generation

A cylinder ($\varnothing = 0.5$ m, height $h = 0.25$ m) with four square electrodes (5 cm edge length) placed equidistantly around the perimeter at mid-height was meshed with Netgen (version 5.3.1) (Schöberl, 1997) and Gmsh (version 4.7.0) (Geuzaine and

Remacle, 2009) meshing software. Current was injected between adjacent electrodes and the voltage was measured between the remaining two electrodes. For 3D meshes an initial analysis was done building on work from Grychtol and Adler (Grychtol and Adler, 2013) where mesh density was set by specifying the maximum edge lengths permitted on electrode surfaces and in the volume of the FEM. Results were compared against those generated using ultra-fine meshes. Calculations were performed with EIDORS (version 3.10) (Adler and Lionheart, 2006) in Matlab 2019b (The Mathworks, Natick, MA, USA).

Meshes of different sizes were generated with Netgen and Gmsh by manipulating the desired maximum edge length (`maxh` parameter) for the entire domain and the electrodes. Two mesh analyses were performed. For the first mesh maximum element lengths were chosen such as to divide the electrode side of 5 cm into an integer number of segments of equal size. The maximum mesh element length ranged from 1 to 7 subdivisions of the electrode edge, while the maximum mesh element length in the ultra-fine reference mesh was 15 subdivisions per electrode edge. Independent reference meshes were generated for each software. Two types of models were generated this way. Constant models C1–C7, where the mesh size was constant, and refined models R1–R7 where the electrode mesh size was specified and dissipated towards an internal mesh element size of 5 cm. Additional refined meshes were generated with reduced mesh size in the internal mesh regions. R1-R7 is referred to as refinement A where the internal element max size was 5 cm. Refinement B had an internal mesh size of 4 cm, C was 3 cm and D was 2 cm. The numeric value in the mesh ID indicated the number of subdivisions per electrode edge. In Netgen the mesh

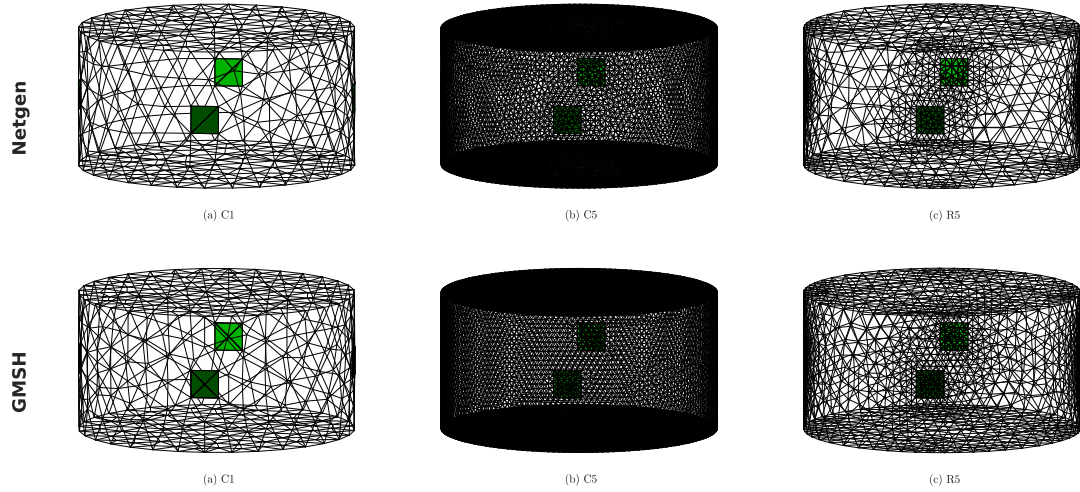


Figure 4.1: Sample meshes generated with Netgen (top row) and Gmsh (bottom row). From left to right: (C1) the coarsest constant mesh; (C5) a refined constant mesh; and (R5) a refined mesh with the same electrode mesh density as C5 but lower internal mesh density.

decay was not controllable, but in Gmsh the size was set to increase evenly from the surface of the electrode to the centre of the model. figure 4.1 shows example meshes of coarse, fine and refined meshes. figure 4.2 on the next page shows the generated mesh structure for constant refinement meshes around the electrode for both Netgen and Gmsh.

For the second analysis, the distribution of nodes within the model was changed without altering the total number of nodes to give M1 – M17. Starting with the constant mesh C3 as M1, the maximum mesh element length on the electrode was decreased by 10% and the maximum mesh size in the centre was increased so that the total number of elements in the mesh was within 10% of the original mesh. C3 was chosen as the starting point because several steps of mesh refinement could be

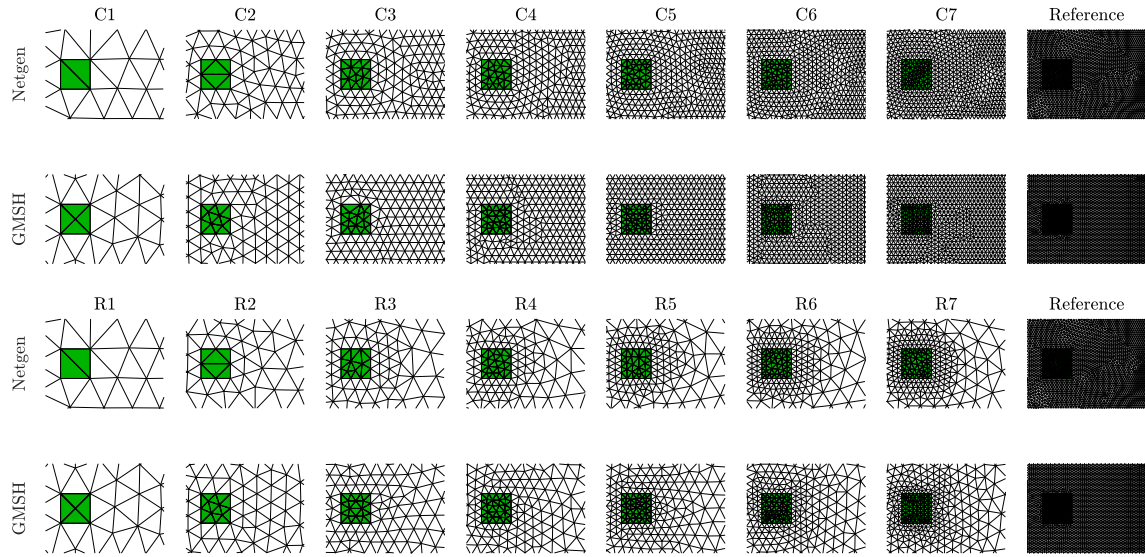


Figure 4.2: A view of the electrode meshing for all constant-density meshes in Netgen and Gmsh. The top two rows show all electrode faces and immediate surrounding surroundings from coarsest (C1) to finest (C7). C represents the constant mesh refinement and the number represents the specified mesh subdivisions per electrode edge. The reference mesh is equivalent to C15. The bottom two rows show refined meshes R1 to R7 with both Netgen and Gmsh and shows the rate of mesh dissipation away from the electrodes.

generated before the electrode mesh density surpassed the reference meshes. For mesh M17 the specified electrode refinement was equal to the reference mesh. In Netgen the mesh dissipation rate was not further controlled, and in Gmsh the mesh density decreased evenly from the electrode surface to the centre of the model. To compare these meshes a section of the model was selected encompassing all points between the centre of the model and a selected electrode face. The average distance, or balance point, along the x-axis of the selected points was expressed as a percentage of the tank radius. This process is illustrated in figure 4.3 on the following page.

When generating meshes to compare across several mesh density profiles as the balance of the nodes was shifted towards the electrodes, 19 meshes were generated for each software including 2 reference meshes. table 4.1 on page 44 shows the parameters of the resulting odd numbered meshes.

4.3.3 Simulation

The potential at each node \mathbf{V} of the mesh was calculated using the finite element method (FEM) using the linearization

$$\mathbf{V} = \mathbf{Y}^{-1}\mathbf{C} \quad (4.1)$$

where \mathbf{Y} is the admittance matrix of the FEM (and a function of conductivity distribution) and \mathbf{C} is a matrix representing the current injection pattern, such that \mathbf{C}_{ij} represents the current injected in electrode i during the j -th stimulation. Here, we drive current of 1 A between two adjacent electrodes in a single stimulation, so

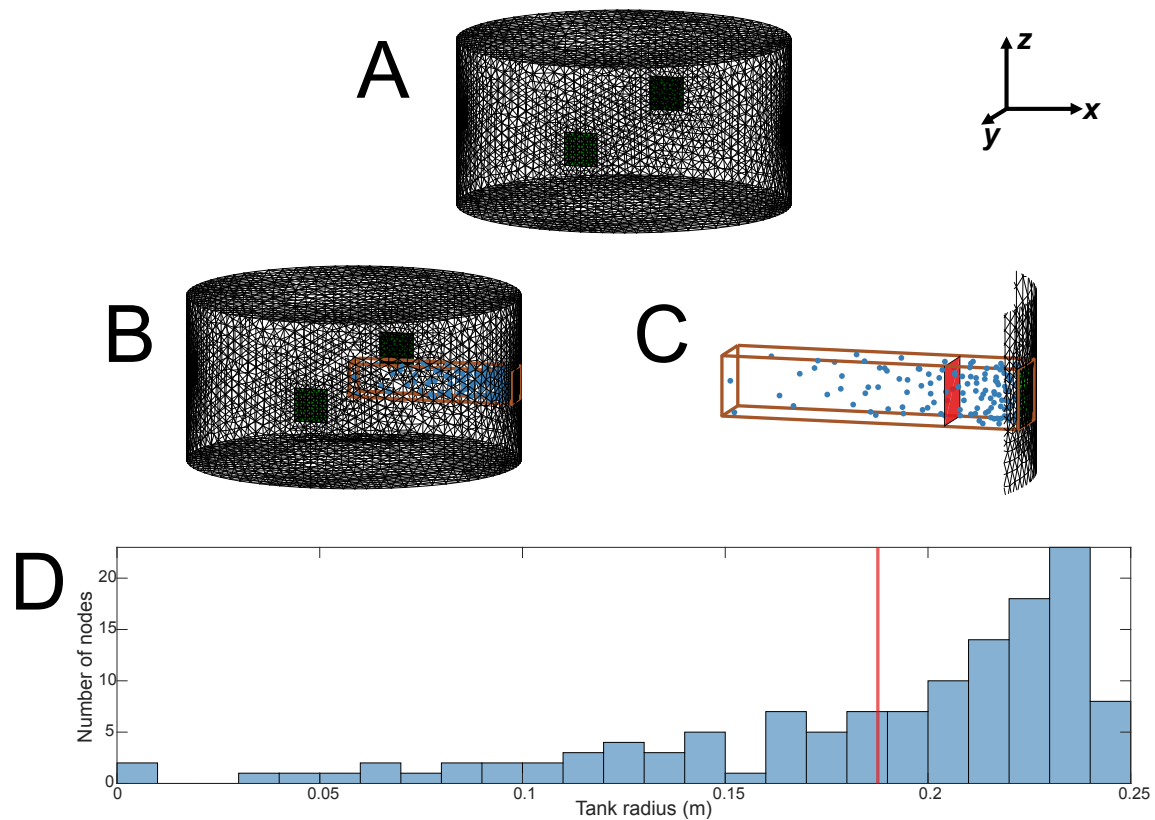


Figure 4.3: A sketch of the process to determine the balance point of generated meshes. A) the starting mesh; B) nodes between the electrode surface and the centre of the model are identified; C) the balance point of the nodes along the x-axis is calculated and indicated by the red plane; D) a histogram showing an example distribution and balance point (red) for the selected model.

Table 4.1: Mesh parameters for odd numbered meshes generated by Netgen (A) and Gmsh (B) to determine the optimal node balance. Parameters global maxh and electrode maxh refer to the specified input parameters; the remaining columns give parameters from the resulting meshes.

Mesh ID		lbl.	elec.	# elem.	# nodes	# elec. elem.	minEL ^a [mm]	maxEL ^b [mm]	minEV ^c [mm ³]	maxEV ^d [mm ³]
M-01	A	16.67	16.67	31347	7095	22	9.80	49.45	254.76	6851.01
	B	16.67	16.67	49210	9615	25	10.32	50.00	222.87	2898.59
M-03	A	18.33	15.00	29639	6482	22	10.75	50.41	289.80	5826.14
	B	18.33	15.00	49247	9680	40	7.36	37.11	172.78	2814.55
M-05	A	18.33	13.33	29814	6589	28	9.39	49.91	162.26	5648.41
	B	20.00	13.33	50749	9930	42	7.80	37.93	134.41	3233.59
M-07	A	18.33	11.67	30581	6723	36	8.77	47.88	141.74	6252.36
	B	21.67	11.67	53002	10429	60	6.17	40.84	63.22	4077.18
M-09	A	18.33	10.00	30690	6755	42	7.86	49.18	115.45	5496.39
	B	23.33	10.00	56237	11008	68	5.82	43.81	62.88	4962.89
M-11	A	18.33	8.33	31575	7030	74	6.05	50.99	60.06	6086.88
	B	26.67	8.33	55545	10886	96	5.51	49.72	36.84	7424.70
M-13	A	20.00	6.67	28589	6447	92	4.65	51.85	20.68	6664.11
	B	30.83	6.67	54993	10825	148	4.51	55.36	20.63	10453.90
M-15	A	21.67	5.00	27775	6245	158	3.46	52.60	11.13	9097.30
	B	36.67	5.00	55331	11000	250	3.51	61.66	7.99	15838.09
M-17	A	30.00	3.33	39116	7590	320	1.75	72.83	1.13	23783.17
	B	48.33	3.33	52947	10798	548	2.32	86.60	2.72	32287.34
REF	A	3.33	3.33	6661789	1173243	510	1.75	9.49	1.01	46.09
	B	3.33	3.33	5871464	976558	554	2.10	7.59	1.58	21.65

a: minimum mesh edge length, *b*: maximum mesh edge length

c: minimum mesh element volume, *d*: maximum mesh element volume

$C = [0 \mid 0 \mid 1 \mid -1]^T$. We pick a node in the centre of the FEM as ground, since it is necessary to assume the potential on one node for \mathbf{Y} to be invertible. We use the complete electrode model and assume contact impedance of 0.01Ω in the calculation of the admittance matrix (Polydorides and McCann, 2002).

We calculate the sensitivity (or Jacobian) matrix \mathbf{J} of measurements \mathbf{v} to changes in the conductivity σ of individual elements as $\mathbf{J}_{ij} = \frac{\partial v_j}{\partial \sigma_i}$ using the adjoint method (Polydorides and McCann, 2002). Again, since we only have one measurement, \mathbf{J} is in fact a vector. We construct a sensitivity image by assigning each element i of the FEM the value of \mathbf{J}_i divided by the element's volume. Mean sensitivity in the plane of electrodes is then calculated by averaging the sensitivity in fifteen planes parallel to the plane of electrodes and spanning the height of 5 cm. The sensitivity was projected onto a 512×512 array and divided into regions of interest for the centre (C), at the electrode (E) and between the centre and electrode (I). The resulting sensitivity for the reference mesh calculated with Gmsh and the selected regions of interest is presented in figure 4.5 on page 48.

4.3.4 Electrode refinement for arbitrary FEMs

Our approach for refinement around electrodes in Gmsh with external electrodes also allows for the refinement of arbitrary models with complex structures such as internal electrodes and tissue boundaries. A scenario depicting an approximation of a probe entering a bone with different layers of conductivity. The resulting mesh pictured in figure 4.7 on page 52 highlights the ability of this technique to be used for refinement around electrodes and the control of mesh density surrounding internal

structures which was previously very challenging in EIT software.

4.4 Results

Two analyses of mesh refinement were completed. The first comparing sensitivity error between meshes with constant refinement and refinement only at the electrodes, and the second comparing meshes with different levels of electrode refinement and the same number of nodes.

When comparing constant meshes to meshes with refinement at the electrodes, sensitivity error was decreased as more nodes were added to the mesh and to the electrodes. The sensitivity error was lowest in the constant meshes across both Netgen and Gmsh software. Meshes generated using Netgen provided a slightly lower sensitivity error relative to the respective reference mesh compared to Gmsh, and resulted in meshes with fewer nodes per electrode given the same input parameters. figure 4.4 on the following page shows the sensitivity error between constant and refined meshes with respect to the number of nodes per electrode.

Example sensitivity profiles for the M-series meshes are shown in figure 4.5 on page 48. The resulting sensitivity profile near the electrodes more closely matched the reference case when refinement at the electrodes was higher.

The total sensitivity error across all meshes is plotted vs. the balance point in figure 4.6 on page 49. For meshes generated with Gmsh the minimum error was achieved when the node balance point was approximately 85% of the model radius corresponding to model M15-B, and for Netgen generated meshes the minimum sensi-

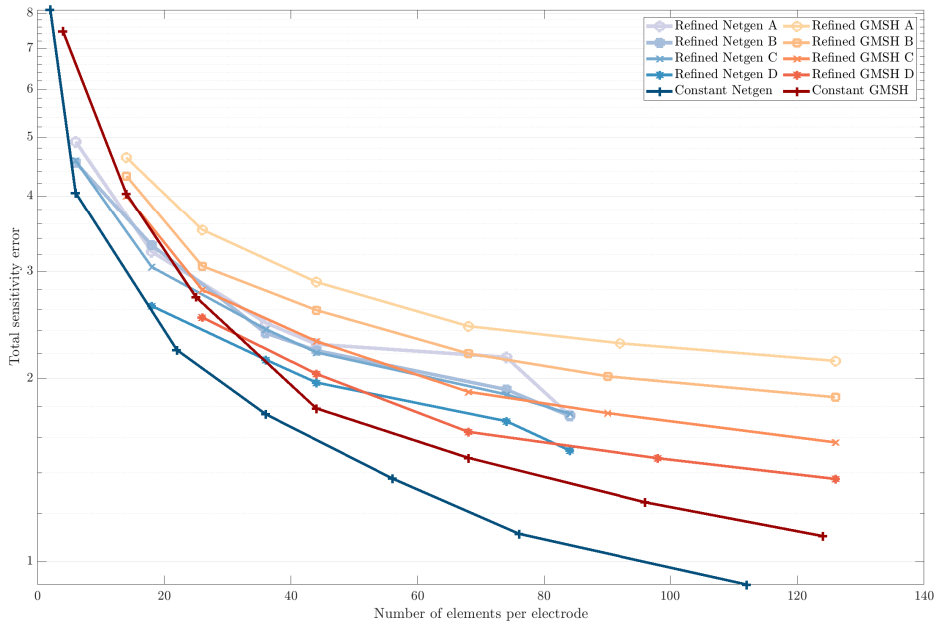


Figure 4.4: Sensitivity error of each mesh as a function of the number of elements per electrode for both Netgen and Gmsh. The darkest lines indicate the constant mesh refinement, lighter lines indicate a larger maximum internal mesh size. The maximum internal mesh sizes are as follows: refinement A - 5 cm; refinement B - 4 cm; refinement C - 3 cm; refinement D - 2 cm.

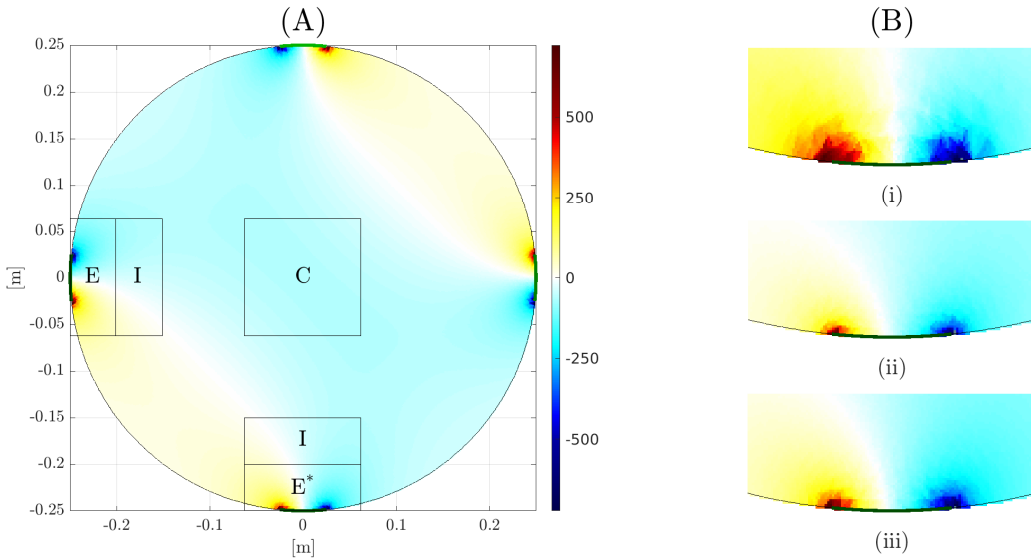


Figure 4.5: (A) Sensitivity distribution for the reference mesh (C15) generated in Gmsh with regions of interest used to compare between models. (B) 3 sensitivity distributions in region E^* next to the electrodes: (i) Constant mesh M1 (ii) refined mesh M15 with a balance point of 82% (iii) reference mesh from (A).

tivity was achieved in model M13-A at a balance point of approximately 70%. Gmsh achieved a lower sensitivity error measured against the respective reference mesh. For meshes using Netgen refinement, the balance point did not increase evenly as the electrode density was increased and the internal density decreased. To maintain the same number of nodes within the model, Gmsh required a larger internal maxh than Netgen. Gmsh generated meshes with more nodes for the same input parameters, but generally the resulting mesh sizes were closer to those specified. The resulting mesh parameters for odd numbered meshes can be seen in table 4.1 on page 44. Across all meshes the measurement error when computing the voltage measurements was insignificant at less than 0.2%.

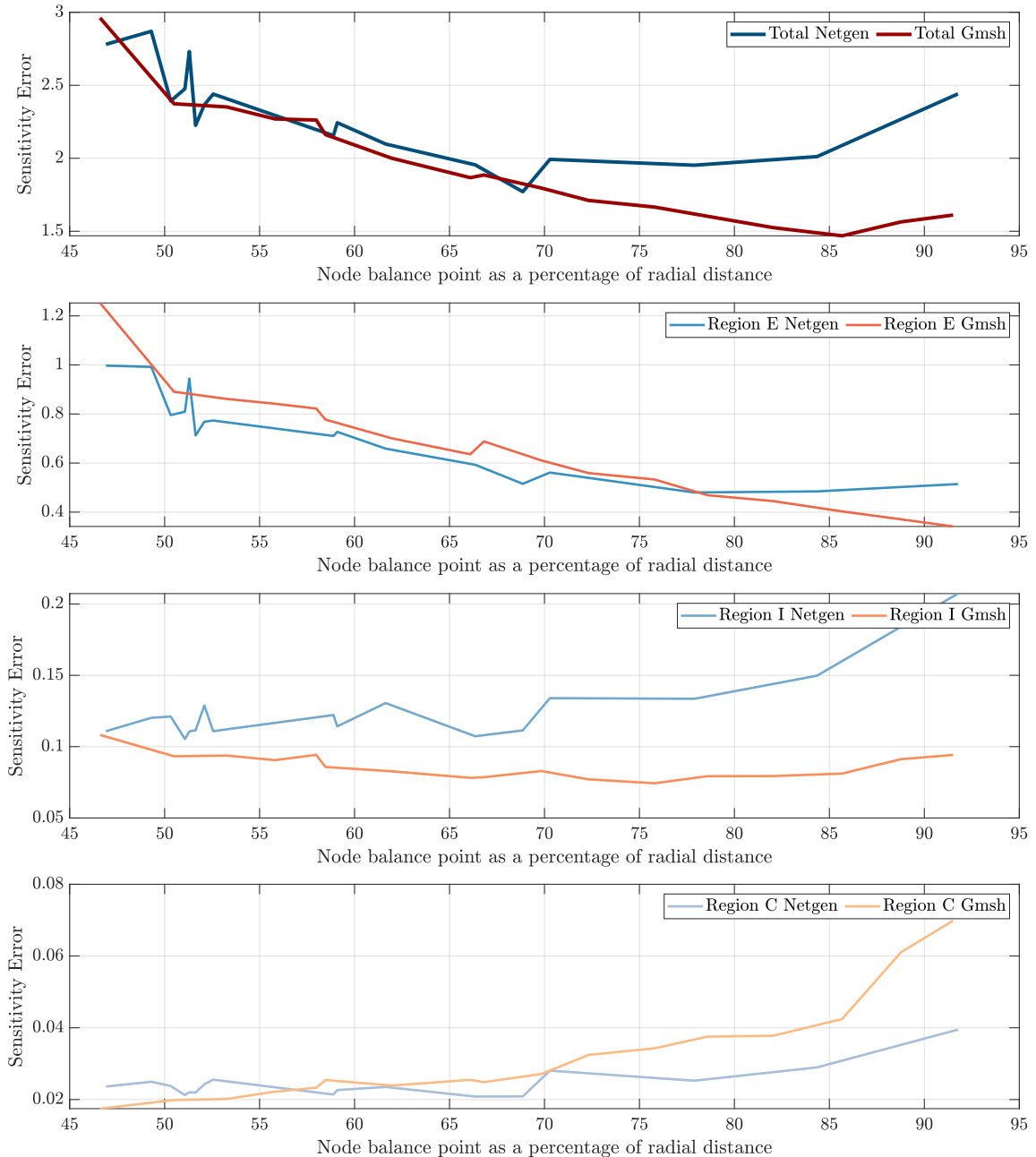


Figure 4.6: Resulting sensitivity error for Netgen (blue) and Gmsh (red) as the balance of the nodes was shifted towards the electrodes. From top to bottom: total sensitivity error, the sum of sensitivity error in region E, the sum of sensitivity error in region I and the sum of sensitivity error in region C. The regions are described in figure 4.5 on the previous page.

4.5 Discussion

We consider several questions on the requirement of FEM refinement in the neighbourhood of electrodes and the available tools for mesh refinement in EIT. 1) Given a “FEM element budget”, what should balance of nodes be between the centre of the model and the electrodes? 2) How do different freely available meshing tools that are commonly used with EIT compare when used to refine 3D meshes?

While refining meshes surrounding the electrodes is agreed to be useful, there is a lack of systematic analysis of the required refinement level, and controlling such refinement is difficult. Automatic mesh refinement is an area of active work and there are a number of commercial and free products available. We compare two programs used widely in EIT. Our results show that Netgen and Gmsh control mesh refinement differently and the same input parameters result in meshes with different numbers of nodes. figure 4.2 on page 41, depicts the difference in mesh dissipation rates between Netgen and Gmsh. The mesh size in Gmsh increased gradually from the surface of the electrode towards the centre of the model, where the mesh size in Netgen increased much more quickly from the edges of the electrode. While we attempted to control the dissipation rate in Netgen by manipulating the mesh density in the centre of the model, we were unable to achieve a smooth transition between the electrode and internal regions of the mesh.

To analyze the benefit of electrode refinement and the difference between Netgen and Gmsh refinement techniques we consider a sequence of refined meshes compared to a “gold standard”, uniformly fine FEM solution. The models were refined either globally or in the electrode neighbourhood, and the error in the sensitivity matrix

J was compared. figure 4.4 on page 47 displays the difference in sensitivity between constant meshes and meshes with refinement at the electrodes. The sensitivity error was lower in Netgen across all constant refinement meshes, in part because there were more total nodes than Gmsh meshes with the same number of nodes on the electrode. Refinement around the electrode decreased the total sensitivity error, but still had larger error than meshes with constant refinement due to the smaller number of nodes in the model.

Using the balance point analysis, we were able to determine the optimal distribution of nodes to minimize sensitivity in both Gmsh and Netgen. The minimum total sensitivity from figure 4.6 on page 49 was approximately 70% for Netgen. This was mainly due to the rapid dissipation of node density away from the electrodes. Increasing the refinement near the electrode reduced error in region E, but in region I there were insufficient nodes to reduce the sensitivity error. As the balance of refinement approached 90% the error in region E also started to increase as the node density did not remain fine throughout the entire region. This effect can also be seen in figure 4.2 on page 41. In Gmsh the optimal balance for refinement was at approximately 85% of the radial distance. Since mesh density was set to reduce evenly between the electrode surface and the centre of the model, there was a higher density of nodes that was maintained in regions E and I as the electrode refinement increased. The error in the centre of the model was higher in Gmsh meshes, but since this is where the sensitivity is lowest the total sensitivity error was much lower.

The ability to selectively control the mesh refinement in regions in Gmsh also allows users to generate complex meshes and control mesh density surrounding internal

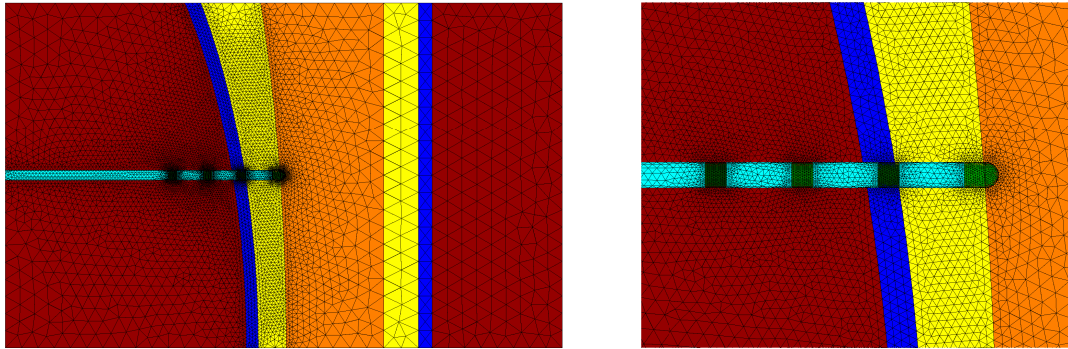


Figure 4.7: Example FEMs of a probe entering a bone from the surrounding tissue. Refinement is specified around the electrodes and tissue interfaces near the probe.

structures and electrodes an example mesh is shown in figure 4.7 where a model was created of a probe entering a bone from the surrounding tissue. These additions fill an important need in EIT to allow for more accurate models of regions surrounding internal structures and electrodes, and

Despite the increased ability to control refinement, the results still show that there are discrepancies between the specified parameters and the resulting meshes. The data in table 4.1 on page 44 show that the maximum element lengths specified for each mesh were different from the actual maximum edge lengths. As the node density was increased near the electrodes, in Netgen the balance point did not always shift towards the electrode as the maximum node density was not always higher despite specifying a smaller mesh size. In Gmsh the mesh density was closer to the specified values, typically resulting in more nodes in the refined meshes.

Across both analyses errors away from the refined areas may be higher, but the ability to refine meshes selectively near regions where high sensitivity is required may allow for reduced measurement error while still allowing for quicker meshing

times. As more electrodes are added and the model complexity is increased, we expect that refinement around the electrodes will continue to reduce total sensitivity error. However the node balance analysis will not be possible for irregularly shaped models. The node balance analysis provides a straightforward method to determine the ideal placement of a given number of nodes to reduce model errors.

4.6 Conclusion

In summary, as expected, refinement of meshes near electrodes does improve model accuracy in terms of sensitivity. We recommend that, for each EIT imaging case, required model accuracy be determined from an analysis of the system, and to minimize the sensitivity error in the forward solution the balance of the nodes should be approximately 85% towards the radius of the model when the dissipation of mesh refinement is constant.

Chapter 5

Custom Meshes from CT Images

5.1 EIT for ARDS Patients

5.2 A Segment Editor Program

5.2.1 Automatic segmentation of the thorax

Algorithm 1: Segment the external body boundary.

Input: image

Output: external boundary

- 1 weiner filter;
 - 2 Set the lung intensity to 0;
 - 3 erode image using disk size 20;
 - 4 reconstruct on image from line 4;
 - 5 dilate with disk of size 20;
 - 6 reconstruct on image from line 6;
 - 7 binarize, thresh = 0.5;
 - 8 fill holes;
 - 9 close - disk of size 2;
 - 10 open using disk size 5;
 - 11 external boundary = largest object;
-

5.2.2 Manual Segmentation Correction

5.2.3 Mesh Generation

5.2.3.1 Extruded Geomerty

5.2.3.2 3D Lung Regions

5.3 Evaluation on ARDS Patients

5.3.1 Methods

5.3.2 Results

Data from 4 ARDS patients with CT and EIT were used to develop a segmentation and correction tool to identify the lungs and boundary of the body. Segmentation was done using the 4th intercostal space, with 10 adjacent CT slices to form an enclosed chest cavity. The lungs and exterior boundary were identified by increasing the contrast and identifying an appropriate threshold. Each segmentation was downsampled to 20 points that could be edited by the user in Matlab. The mesh was generated using `ng_mk_extruded_model Grychtol2012` in EIDORS 3.10 **Adler2019**. Images were reconstructed using GREIT **Adler2009**. The GI index was calculated using the method presented by Zhao et al. **Zhao2009** using the lung regions from the forward model. A ventilated lung estimate was made using the segmentation as $\frac{A_{\text{ventilated lung}}}{A_{\text{total lung}}}$.

Results in fig. figure ?? on page ?? show a reconstructed image with more separable lungs in the enhanced model, and a mean GI index for each breath in the 1 minute recording that follows trend of the ventilated lung percentage in table 5.1.

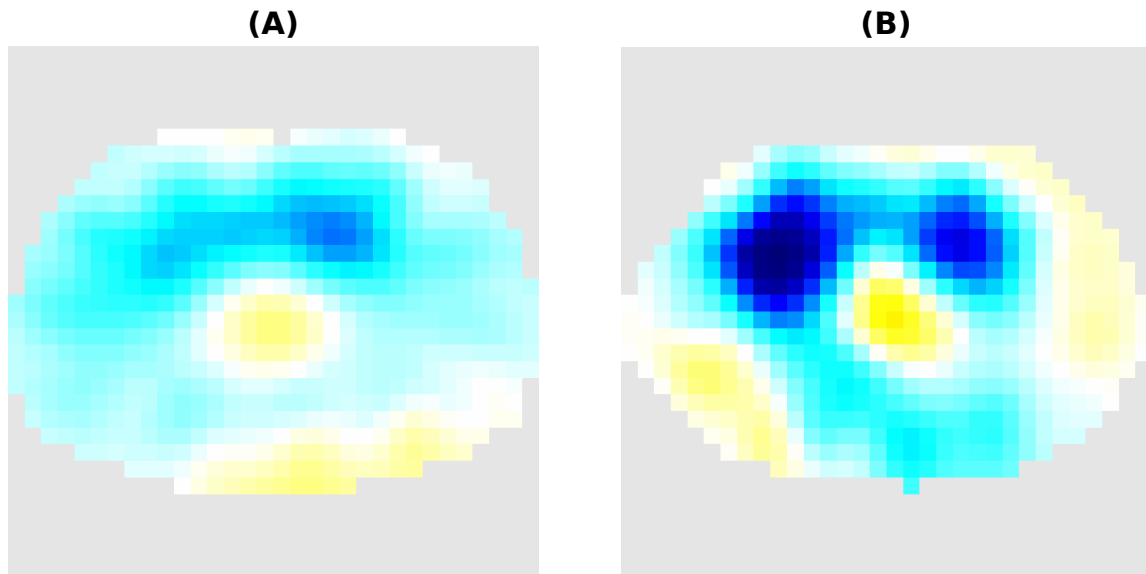


Figure 5.1: Single breath using: A) generic model B) custom model

Table 5.1: Ventilated lung estimate vs. GI index scores.

Sub- ject	Venti- lated lung (%)	GI (basic model)	GI (cus- tom model)
1	99.9	0.353±0.00	40.690±0.005
2	85.5	0.640±0.02	20.771±0.020
3	79.6	0.695±0.00	70.857±0.009
4	27.0	0.614±0.01	11.81±0.053

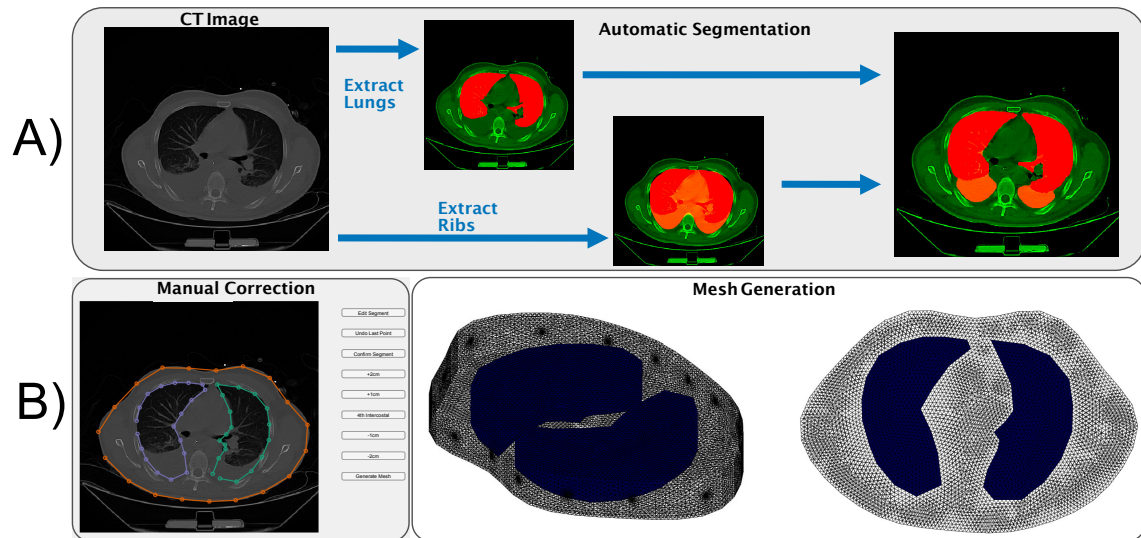


Figure 5.2: An overview of the segmentation and editing process showing: A) A sample raw CT which was thresholded, scaled and adjusted over several adjacent slices to identify the lung regions and an enclosed rib area, and the resulting lung estimate; and B) A screen capture of the manual mesh correction process and 2 views of the generated mesh.

Chapter 6

Internal Electrodes

6.1 Motivation

One of the shortcomings of EIT is low sensitivity away from the electrodes. For continuous monitoring of cardiac-related events an EIT protocol with an improved sensitivity near the heart and innermost regions of the lungs may improve results and imaging accuracy.

EIT has low sensitivity away from the electrodes which are typically placed on the body surface. This chapter will investigate the use and application of internal electrodes and quantify the improvement in sensitivity and image reconstruction accuracy in simulation.

6.2 Summary

This chapter provides proof of principle of internal electrode configurations to improve EIT sensitivity and reconstruction accuracy. The goal of this chapter is to determine the viability of internal electrode use through a series of simulations and phantom measurements then validate the imaging ability using one or two animals.

We expect to show that using internal electrodes increases the sensitivity of the measurements to internal impedance changes and enables a higher resolution of image reconstructions in these central regions of the thorax.

6.3 Simulations

To analyze the sensitivity changes due to different electrode configurations finite element models (FEMs) of a cylindrical tank were created with each of the tested electrode configurations. Figure 6.1 shows the four different configurations that were tested: a 2D electrode ring of 32 electrodes; a 3D configuration of 2 layers of 16 electrodes (3D(a)); a second 3D configuration of 2 layers of 15 electrodes plus 2 central internal electrodes inline with the electrode planes (3D(b)); and a final 3D configuration of 2 layers of 14 electrodes with 4 central internal electrodes evenly spaced between the electrode planes (3D(c)).

The tank in the simulations has a height of 2 m, radius of 1 m, and the electrode radius is 0.05 m for both the round external electrodes and the spherical internal electrodes. In the 3D configurations the plane separation is 0.5 m and in all configurations the radial spacing between electrodes is equal. The background conductivity

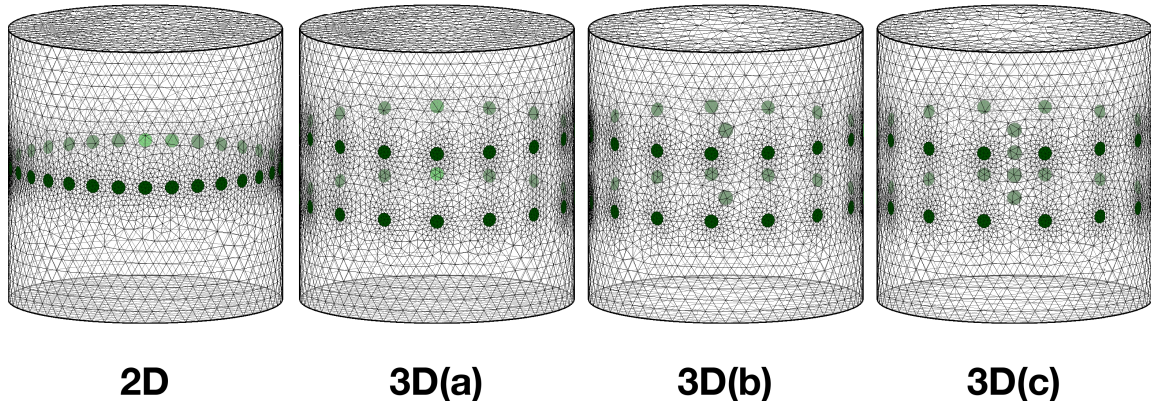


Figure 6.1: 4 configurations of electrodes were tested: 2D) a single ring of 32 electrodes; 3D(a) 2 rows of 16 external electrodes; 3D(b) 2 rows of 15 external electrodes with 2 internal electrodes; and 3D(c) 2 rows of 14 external electrodes and 4 internal electrodes.

of the tank was 1 S/m and the conductivity of the target was 10 S/m.

When reconstructing images a conductive target was added to the tank centred at a height of 1 m at the midpoint of the tank radius. The target object radius is 0.4 m.

The reconstructions of the conductive object with and without additive noise are shown in Figure 6.2. To generate EIT images from voltage measurements, the 3D GREIT reconstruction algorithm was used (**Adler2009**). A spherical conductive target with a radius of 20% of the tank radius was placed midway between the centre and boundary of the tank, in a region with typically low sensitivity. The inverse problem hyperparameter was selected so that in all instances the amount of measurement noise that propagated from the measurements into the final images was equal.

Preliminary reconstructions on simulated data show that internal electrodes are able to reconstruct a conductive object closer to its true size based on visual inspec-

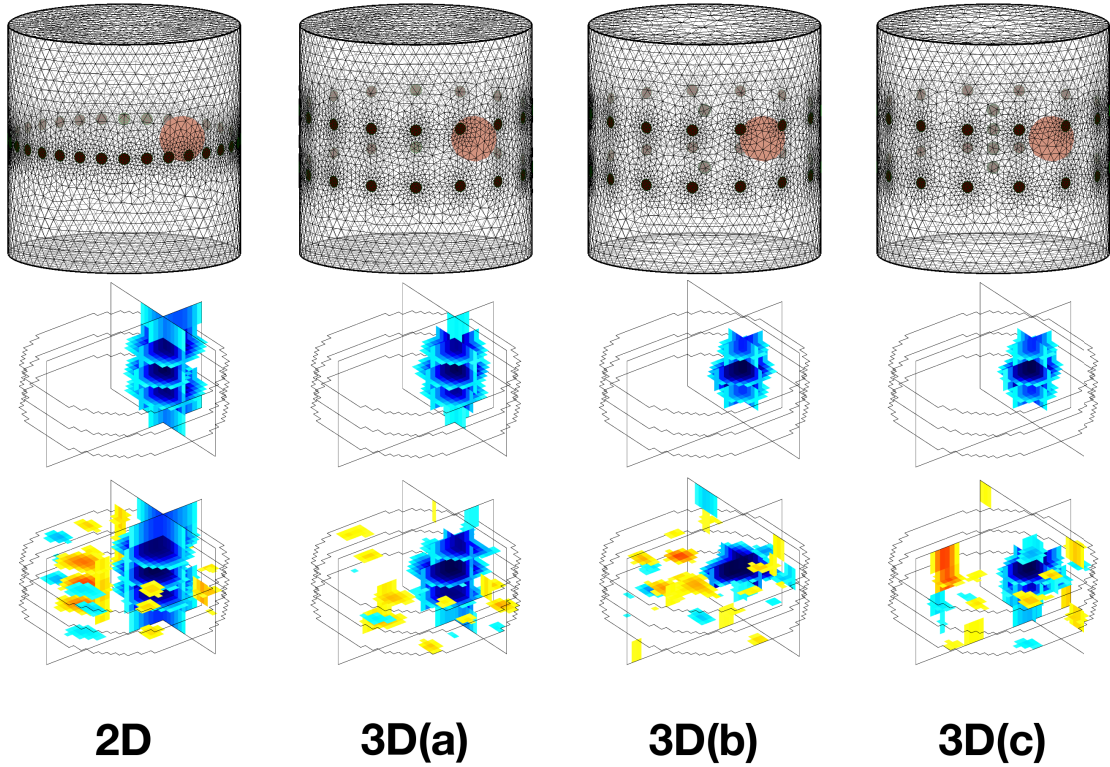


Figure 6.2: The top row shows reconstructions with no additive noise, and the second row shows reconstructions on measurements with 5dB of additive noise.

tion, but more simulations are required to quantify the improvements. These preliminary reconstructions are shown in Figure 6.2. The top row shows reconstructions with no additive noise, and the second row shows reconstructions on measurements with 5dB of additive noise.

Preliminary results shown in Figure 6.3 show internal sensitivity distribution changes when using 2 and 4 internal electrodes compared to the typical 2D and 3D configurations with only external electrodes.

The sensitivity is then calculated from the jacobian (J) of the reconstruction ma-

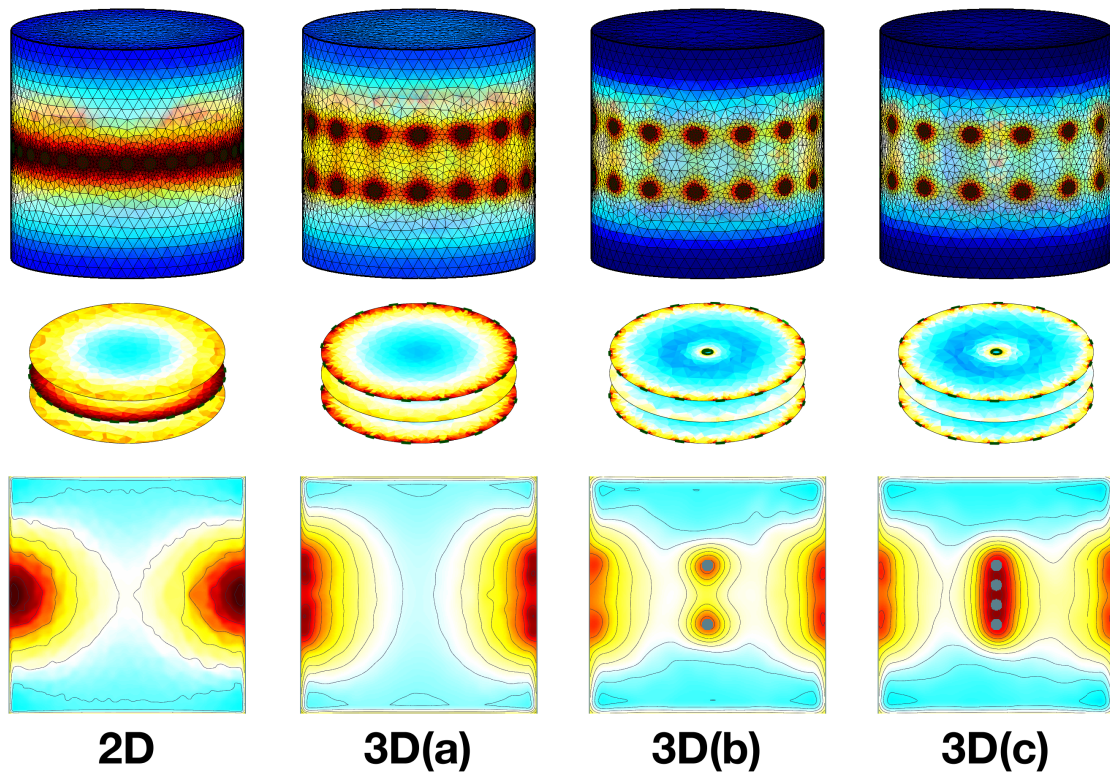


Figure 6.3: Sensitivity distributions for electrode patterns from left to right: A single 2D electrode plane; 2 electrode planes of 16 electrodes each; 2 internal electrodes and 2 external electrode rings of 15 electrodes; 4 internal electrodes arranged between 2 planes of 14 external electrodes

trix as:

$$S = \frac{\sqrt{\sum_i \vec{J}_{ij}^2}}{V_i}$$

where V_i is the volume of each respective voxel.

These results show the expected increased sensitivity in the central regions of the model. To further improve internal sensitivity a new measurement pattern is proposed that uses more measurements between the internal probe and peripheral electrodes. The proposed injection and measurement pattern is shown in Figure 6.4. The sensitivity of the proposed pattern was compared to the sensitivity profile of the same configuration using the basic “skip 4” injection and measurement pattern which has been found to give good sensitivity in 2D and 3D external electrode configurations **Grychtol2016**.

Using this injection pattern preliminary results show a further increase in sensitivity in the internal regions without increasing the measurement acquisition time. The sensitivity distribution for the new injection pattern is pictured in Figure 6.5.

To quantify image quality, the same object will be reconstructed in multiple situations and is computed as a combination of the following metrics: mean squared error (MSE) between the reconstructed object and the actual geometry; full width half max (FWHM) of the reconstructed object; and separability of two identical circular objects in the same reconstruction.

Building on this work simulations will be used to answer more questions on the use of internal electrodes:

- What internal electrode configuration most improves the internal sensitivity?
- What is the best injection pattern for measuring activity in the heart region?

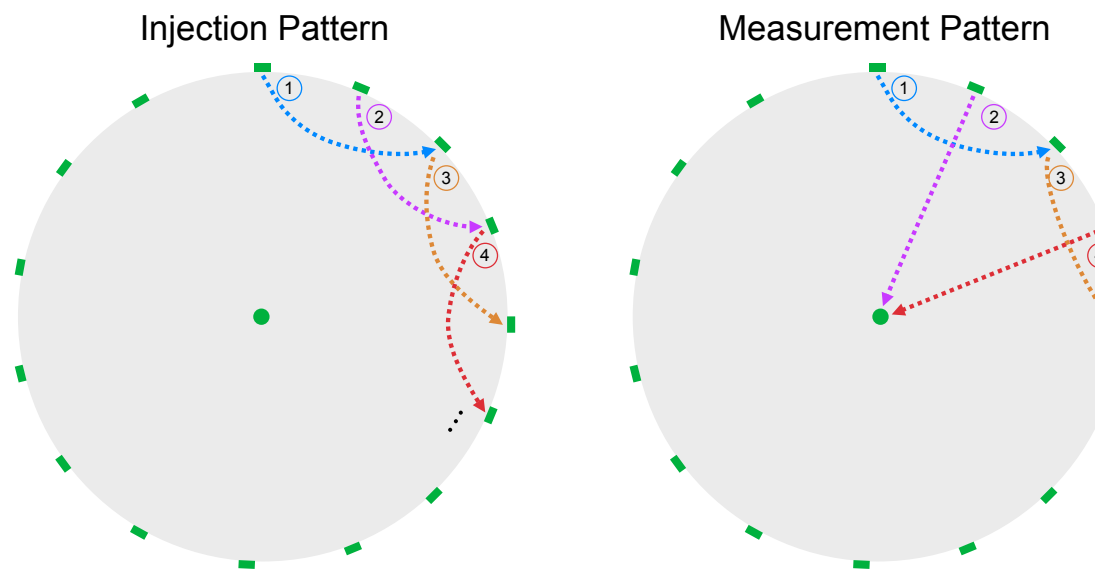


Figure 6.4: A proposed current injection and measurement pattern for EIT imaging with 2 internal electrodes. The injection pattern is a typical “skip 4” pattern injecting between every 5th electrode in a square electrode layout and the measurement pattern replaces every 2nd measurement in the typical method with a measurement between the internal probe and external rings. Note: this figure does not differentiate between upper and lower electrode planes, but all injections and measurements are done between the 2 planes.

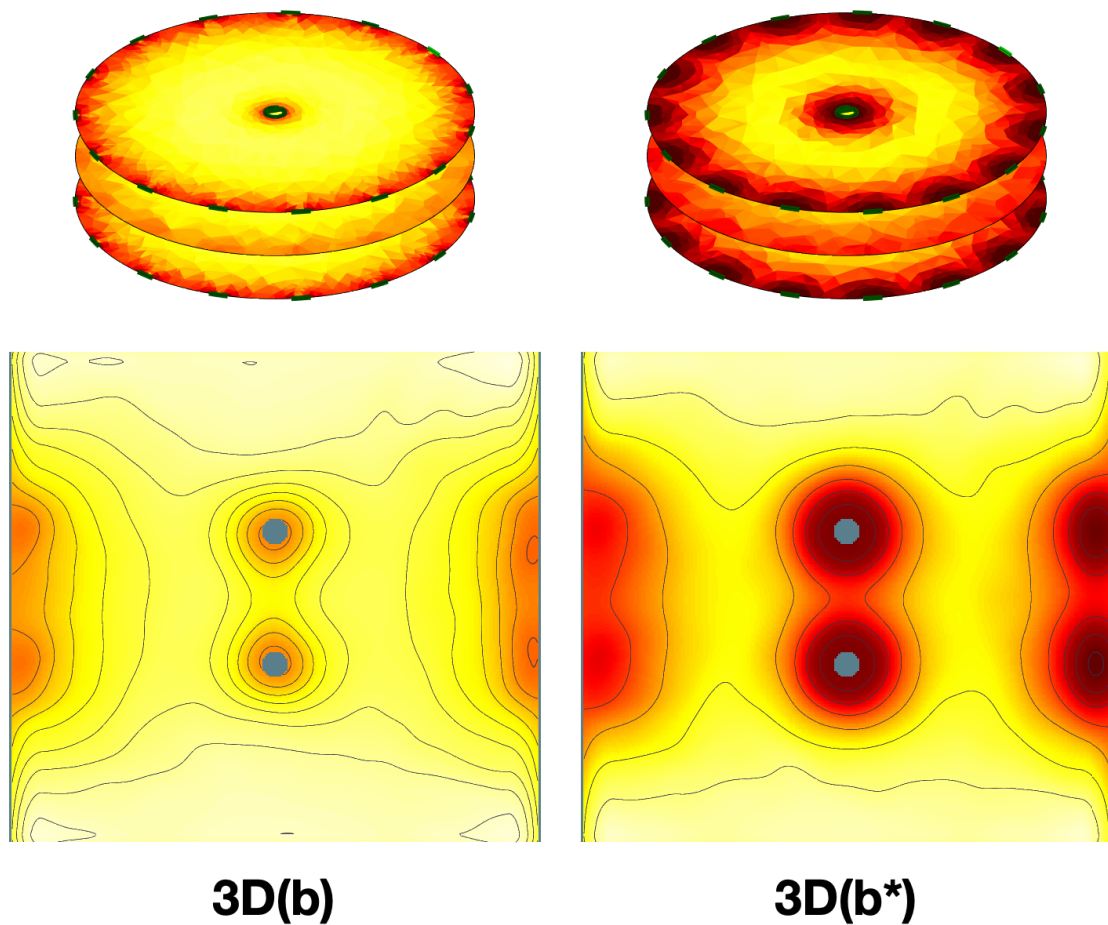


Figure 6.5: A comparison between the sensitivity distributions for a typical “skip 4” injection pattern pictured on the left (3D(b)) and the modified injection and measurement pattern on the right (3D(b^{*})).

- What is the maximum number of electrodes that can be placed internally while maintaining image quality?
- How should internal electrodes be used for current injections?
- How sensitive is the resulting image to movement of the internal electrodes?
- In what regions of the FEM is the object reconstruction improved?
- Do internal electrodes pose any risk to patient safety?

6.4 Phantom Measurements

Phantom measurements are used to asses the real-world performance of the measurements and configurations that were identified in simulations. Two non-conductive circular objects are placed and imaged at 4 different separations: 1 cm, 6 cm, 11 cm and 16 cm mid-way between the central probe and the tank wall. These separations are used to determine the change in resolution between the different configurations.

In addition to determining the real-world separability the phantom measurements will be used to image a conductive object in a region representing the heart region and determine the FWHM and MSE based on the measured location of the object within the phantom dimensions. This will be compared to the results obtained through simulations.

6.5 Motion Correction

6.6 Inverse Source Localization

6.7 Animal Data

Internal electrodes present the opportunity to obtain a significantly higher sensitivity and with motion correction may be used to give a more accurate estimate of arterial pressure. This paper presents a method of using internal electrodes while correcting for motion of the internal probe to yield high sensitivity near to the esophageal probe.

6.8 Methods

The forward model was constructed using EIDORS version 3.10 **Adler2019** using `mk_library_model` **Grychtol2012** the internal electrode was added as an extra structure. This model was also used to identify the heart and lung regions. The sensitivity of the lamb model was calculated from the Jacobian using the method from **Stowe2020**. Sensitivity profiles using 32 electrodes with and without 4 internal electrodes are shown in fig. 6.6.

Data were collected in 3 ewes during ventilation under general anesthetic using the SenTec EIT Pioneer Set. 30 second recordings were made during regular ventilation with a volume of 400 ± 50 ml, frequency of 0.2 ± 0.05 Hz, and peep of 6. Recordings were repeated for several ventilation scenarios including: high volume (+100 ml), low volume (-100 ml), high frequency (+0.17 Hz), low frequency (0.07 Hz), high peep

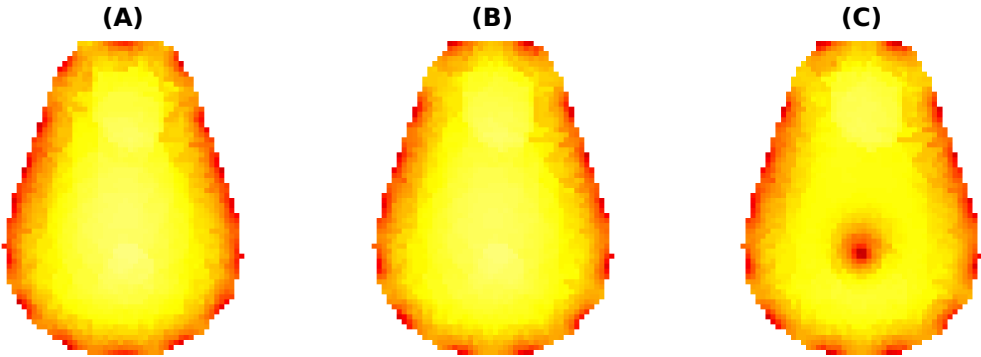


Figure 6.6: Sensitivity distribution averaged across 10 evenly spaced layers between the electrode planes in the lamb model for: A) 32 external electrodes B) 28 external electrodes c) 28 external electrodes and 4 internal electrodes

(10) and low peep (4).

All breaths in each 30 second segment were ensemble averaged to give one representative breath for each scenario.

Images of one averaged breath per recording were reconstructed using the 3D GREIT algorithm **bartek2016** which minimizes the effect of electrode motion on the resulting image. Results were compared for both external only and internal electrode configurations using the same recording. To obtain results with only external electrodes all injections and measurements using internal electrodes were removed prior to reconstruction. Measurements on injecting electrodes were always removed. Images from subject 3 during regular ventilation are shown below in fig. 6.7. With internal electrodes impedance changes at the cardiac frequency had a magnitude of $6.4\% \pm 4.35\%$ of the ventilation frequency and without internal electrodes the amplitude of the cardiac frequency was $0.8\% \pm 0.3\%$ of the ventilation frequency signal.

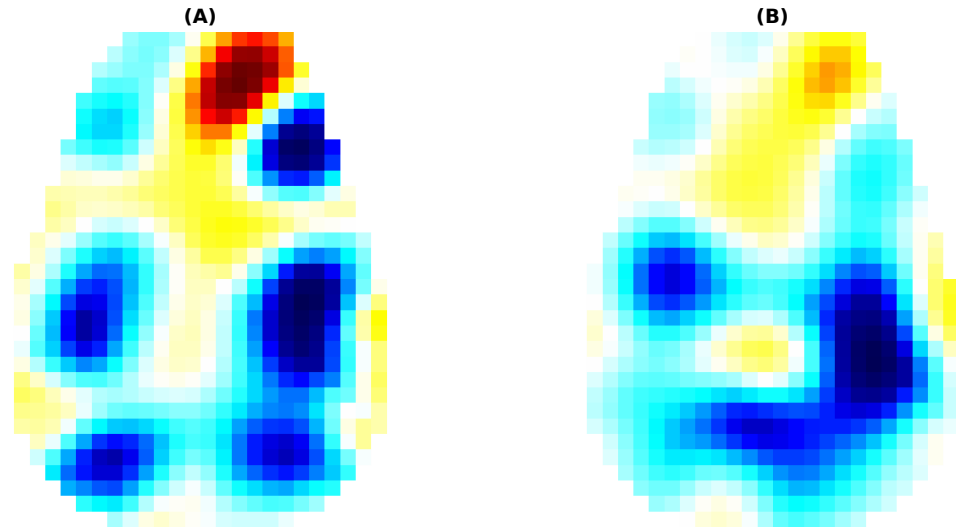


Figure 6.7: A single breath imaged with: A) no current injections or measurements on internal electrodes b) with internal electrodes

6.9 Conclusions

Reconstructions using the GREIT algorithm with internal electrodes on an esophageal probe were able to give increased sensitivity to cardiac-frequency impedance changes and may allow for better measures of blood pressure and pulse wave velocity.

Chapter 7

Conclusion

7.1 Summary of Findings

7.2 Future Work

Bibliography

- Adler, A., Boyle, A., Crabb, M. G., Grychtol, B. L., Lionheart, W. R. B., Tregidgo, H. F. J., & Yerworth, R. (2017). EIDORS version 3.9 [Conference Name: Proceedings of the 18th International Conference on Biomedical Applications of Electrical Impedance Tomography (EIT) Meeting Name: Proceedings of the 18th International Conference on Biomedical Applications of Electrical Impedance Tomography (EIT) Publisher: Thayer School of Engineering at Dartmouth]. *Proc. 18th Int. Conf. on Biomed. Applications of EIT*.
- Adler, A., Amato, M. B., Arnold, J. H., Bayford, R., Bodenstein, M., Böhm, S. H., Brown, B. H., Frerichs, I., Stenqvist, O., Weiler, N., & Wolf, G. K. (2012). Whither lung EIT: Where are we, where do we want to go and what do we need to get there? [Publisher: IOP Publishing]. *Physiological Measurement*, 33(5), 679–694.
- Adler, A., Arnold, J. H., Bayford, R., Borsic, A., Brown, B., Dixon, P., Faes, T. J. C., Frerichs, I., Gagnon, H., Gärber, Y., Grychtol, B., Hahn, G., Lionheart, W. R. B., Malik, A., Patterson, R. P., Stocks, J., Tizzard, A., Weiler, N., & Wolf, G. K. (2009). GREIT: A unified approach to 2d linear EIT reconstruction of lung images [Publisher: IOP Publishing]. *Physiological Measurement*, 30(6), S35–S55.
- Adler, A., & Boyle, A. (2017). Electrical impedance tomography: Tissue properties to image measures [Conference Name: IEEE Transactions on Biomedical Engineering]. *IEEE Transactions on Biomedical Engineering*, 64(11), 2494–2504.
- Adler, A., & Lionheart, W. R. B. (2006). Uses and abuses of EIDORS: An extensible software base for EIT [Publisher: IOP Publishing]. *Physiological Measurement*, 27(5), S25–S42.
- Allaud, L., & Martin, M. (1977). *Schlumberger: The history of a technique*. Wiley.
- Bartocci, M., Serra, G., Basano, L., Canepa, F., & Ottonello, P. (1999). Cerebral blood-flow monitor for use in neonatal intensive care units. *Computer Methods and Programs in Biomedicine*, 59(1), 61–73.

- Bhuyan, U., Peters, A. M., Gordon, I., Davies, H., & Helms, P. (1989). Effects of posture on the distribution of pulmonary ventilation and perfusion in children and adults. [Publisher: BMJ Publishing Group Ltd Section: Research Article]. *Thorax*, 44(6), 480–484.
- Borges, J. B., Suarez-Sipmann, F., Bohm, S. H., Tusman, G., Melo, A., Maripuu, E., Sandström, M., Park, M., Costa, E. L. V., Hedenstierna, G., & Amato, M. (2012). Regional lung perfusion estimated by electrical impedance tomography in a piglet model of lung collapse [Publisher: American Physiological Society]. *Journal of Applied Physiology*, 112(1), 225–236.
- Braun, F., Proença, M., Adler, A., Riedel, T., Thiran, J.-P., & Solà, J. (2018). Accuracy and reliability of noninvasive stroke volume monitoring via ECG-gated 3d electrical impedance tomography in healthy volunteers [Num Pages: e0191870 Place: San Francisco, United States Publisher: Public Library of Science Section: Research Article]. *PLoS One*, 13(1), e0191870.
- Cohen, J. (1977). *Statistical power analysis for the behavioral sciences* (Revised edition.). Academic Press.
- Deibele, J. M., Luepschen, H., & Leonhardt, S. (2008). Dynamic separation of pulmonary and cardiac changes in electrical impedance tomography [Publisher: IOP Publishing]. *Physiological Measurement*, 29(6), S1–S14.
- Ericsson, E., Tesselaar, E., & Sjöberg, F. (2016). Effect of electrode belt and body positions on regional pulmonary ventilation- and perfusion-related impedance changes measured by electric impedance tomography [Num Pages: e0155913 Place: San Francisco, United States Publisher: Public Library of Science Section: Research Article]. *PLoS One*, 11(6), e0155913.
- Eyüboğlu, B., Brown, B., & Barber, D. (1989). In vivo imaging of cardiac related impedance changes [Conference Name: IEEE Engineering in Medicine and Biology Magazine]. *IEEE Engineering in Medicine and Biology Magazine*, 8(1), 39–45.
- Ferrario, D., Grychtol, B., Adler, A., Sola, J., Bohm, S. H., & Bodenstein, M. (2012). Toward morphological thoracic EIT: Major signal sources correspond to respective organ locations in CT [Conference Name: IEEE Transactions on Biomedical Engineering]. *IEEE Transactions on Biomedical Engineering*, 59(11), 3000–3008.
- Frerichs, I., Hinz, J., Herrmann, P., Weisser, G., Hahn, G., Quintel, M., & Hellige, G. (2002). Regional lung perfusion as determined by electrical impedance tomography in comparison with electron beam CT imaging [Conference Name: IEEE

- Transactions on Medical Imaging]. *IEEE Transactions on Medical Imaging*, 21(6), 646–652.
- Frerichs, I., Amato, M. B. P., Kaam, A. H. v., Tingay, D. G., Zhao, Z., Grychtol, B., Bodenstein, M., Gagnon, H., Böhm, S. H., Teschner, E., Stenqvist, O., Mauri, T., Torsani, V., Camporota, L., Schibler, A., Wolf, G. K., Gommers, D., Leonhardt, S., Adler, A., & Group, T. s. (2017). Chest electrical impedance tomography examination, data analysis, terminology, clinical use and recommendations: Consensus statement of the TRanslational EIT developmeNt stuDy group [Publisher: BMJ Publishing Group Ltd Section: State of the art review]. *Thorax*, 72(1), 83–93.
- Fu, S. X., Lai, K. L., Si, Y. T., Xu, L., Xiao, M. D., & Gang, A. (1996). Study of the safe threshold of apneic period in children during anesthesia induction [Publisher: Elsevier Science]. *Journal of Clinical Anesthesia*, 8(7), 568–574.
- Geuzaine, C., & Remacle, J.-F. (2009). Gmsh: A 3-d finite element mesh generator with built-in pre- and post-processing facilities [Publisher: John Wiley & Sons, Ltd.]. *International Journal for Numerical Methods in Engineering*, 79(11), 1309–1331.
- Grychtol, B., & Adler, A. (2013). FEM electrode refinement for electrical impedance tomography. *2013 35th Annual International Conference of the IEEE Engineering in Medicine and Biology Society (EMBC)*, 6429–6432.
- Grychtol, B., Lionheart, W. R. B., Bodenstein, M., Wolf, G. K., & Adler, A. (2012). Impact of model shape mismatch on reconstruction quality in electrical impedance tomography [Conference Name: IEEE Transactions on Medical Imaging]. *IEEE Transactions on Medical Imaging*, 31(9), 1754–1760.
- Grychtol, B., Müller, B., & Adler, A. (2016). 3d EIT image reconstruction with GREIT [Publisher: IOP Publishing]. *Physiological Measurement*, 37(6), 785–800.
- Halter, R., Hartov, A., & Paulsen, K. (2008). Imaging forearm blood flow with pulse-ox gated electrical impedance tomography [ISSN: 1558-4615]. *2008 30th Annual International Conference of the IEEE Engineering in Medicine and Biology Society*, 1192–1195.
- Leathard, A. D., Brown, B. H., Campbell, J., Zhang, F., Morice, A. H., & Tayler, D. (1994). A comparison of ventilatory and cardiac related changes in EIT images of normal human lungs and of lungs with pulmonary emboli [Publisher: IOP Publishing]. *Physiological Measurement*, 15(2), A137–A146.

- Leonhardt, S., & Lachmann, B. (2012). Electrical impedance tomography: The holy grail of ventilation and perfusion monitoring? *Intensive Care Medicine*, 38(12), 1917–1929.
- Moens, Y., Schramel, J. P., Tusman, G., Ambrisko, T. D., Solà, J., Brunner, J. X., Kowalczyk, L., & Böhm, S. H. (2014). Variety of non-invasive continuous monitoring methodologies including electrical impedance tomography provides novel insights into the physiology of lung collapse and recruitment – case report of an anaesthetized horse [Publisher: Elsevier]. *Veterinary Anaesthesia and Analgesia*, 41(2), 196–204.
- Nakazato, R., Tamarappoo, B. K., Kang, X., Wolak, A., Kite, F., Hayes, S. W., Thomson, L. E. J., Friedman, J. D., Berman, D. S., & Slomka, P. J. (2010). Quantitative upright-supine high-speed SPECT myocardial perfusion imaging for detection of coronary artery disease: Correlation with invasive coronary angiography [Num Pages: 8 Place: New York, United States Publisher: Society of Nuclear Medicine]. *The Journal of Nuclear Medicine*, 51(11), 1724–31.
- Nguyen, D. T., Bhaskaran, A., Chik, W., Barry, M. A., Pouliopoulos, J., Kosobrodov, R., Jin, C., Oh, T. I., Thiagalingam, A., & McEwan, A. L. (2015). Perfusion redistribution after a pulmonary-embolism-like event with contrast enhanced EIT [Publisher: IOP Publishing]. *Physiological Measurement*, 36(6), 1297–1309.
- Nguyen, D. T., Jin, C., Thiagalingam, A., & McEwan, A. L. (2012). A review on electrical impedance tomography for pulmonary perfusion imaging [Publisher: IOP Publishing]. *Physiological Measurement*, 33(5), 695–706.
- Polydorides, N., & McCann, H. (2002). Electrode configurations for improved spatial resolution in electrical impedance tomography [Publisher: IOP Publishing]. *Measurement Science and Technology*, 13(12), 1862–1870.
- Proença, M., Braun, F., Solà, J., Thiran, J.-p., & Lemay, M. (2017). Noninvasive pulmonary artery pressure monitoring by EIT: A model-based feasibility study [Num Pages: 949-963 Place: Heidelberg, Netherlands Publisher: Springer Nature B.V.]. *Medical and Biological Engineering and Computing*, 55(6), 949–963.
- Reifferscheid, F., Elke, G., Pulletz, S., Gawelczyk, B., Lautenschläger, I., Steinfath, M., Weiler, N., & Frerichs, I. (2011). Regional ventilation distribution determined by electrical impedance tomography: Reproducibility and effects of posture and chest plane [Publisher: Blackwell Publishing Asia]. *Respirology*, 16(3), 523–531.

- Sage, M., Nadeau, M., Forand-Choinière, C., Mousseau, J., Vandamme, J., Berger, C., Tremblay-Roy, J.-S., Tissier, R., Micheau, P., & Fortin-Pellerin, É. (2018). Assessing the impacts of total liquid ventilation on left ventricular diastolic function in a model of neonatal respiratory distress syndrome [Num Pages: e0191885 Place: San Francisco, United States Publisher: Public Library of Science Section: Research Article]. *PLoS One*, 13(1), e0191885.
- Schöberl, J. (1997). NETGEN an advancing front 2d/3d-mesh generator based on abstract rules. *Computing and Visualization in Science*, 1(1), 41–52.
- Solà, J., Adler, A., Santos, A., Tusman, G., Sipmann, F. S., & Bohm, S. H. (2011). Non-invasive monitoring of central blood pressure by electrical impedance tomography: First experimental evidence [Num Pages: 409-15 Place: Heidelberg, Netherlands Publisher: Springer Nature B.V.]. *Medical and Biological Engineering and Computing*, 49(4), 409–15.
- Zadehkoochak, M., Blott, B. H., Hames, T. K., & George, R. F. (1992). Pulmonary perfusion and ventricular ejection imaging by frequency domain filtering of EIT images [Publisher: IOP Publishing]. *Clinical Physics and Physiological Measurement*, 13, 191–196.